Energy 282 (2023) 128740

Contents lists available at ScienceDirect

Energy

journal homepage: www.elsevier.com/locate/energy

Numerical modeling and parametric study of the heat storage process of the 1.05 MW molten salt furnace

Xue Xue [a], Xiang Liu [a], Yifan Zhu [a], Lei Yuan [b], Ying Zhu [c], Kelang Jin [a], Lei Zhang [a], Hao Zhou [a,*]

[a] Zhejiang University, Institute for Thermal Power Engineering, State Key Laboratory of Clean Energy Utilization, Hangzhou, 310027, PR China
[b] China Shipbuilding New Power Co., Ltd, Haidian District, Beijing, PR China
[c] Shanghai Zhenshi Energy Technology Co., Ltd, Yangpu District, Shanghai, PR China

ARTICLE INFO

Handling Editor: A. Olabi

Keywords:
Thermal energy storage
Molten salt furnace
Non-stationary
Thermal performance analysis

ABSTRACT

The implementation of thermal storage technology in the steel industry has the potential to reduce carbon emissions and contribute to a more sustainable future for the planet. Utilizing molten salt furnaces to convert waste heat from blast furnace gas into thermal energy from molten salt is an innovative approach. In this study, the heat flux density data calculated using ANSYS FLUENT were imported into a MATLAB calculation program developed based on the multi-section lumped parameter method to model the three-dimensional transient thermal performance calculations of the molten salt furnace. A benchmark energy storage experiment on a 1.05 MW furnace validated simulation results. The experimental molten salt outlet temperature is 566.5 °C, 13.92 °C higher than the simulation data with 2.46% deviation. The study investigates the dynamic characteristics of thermal energy storage in molten salt furnaces by disturbing external parameters. Results show that molten salt temperature rise is linearly related to heat flux density, molten salt inlet temperature, and mass flow rate. Notably, every 0.8 kg/s increase in molten salt mass flow rate reduces the outer coil temperature by 6.59%. The highly accurate model provides a reference for the design, control and commissioning of molten salt heating and thermal storage systems.

1. Introduction

The significant increase in global energy consumption poses enormous challenges to the energy system [1]. Storing excess energy and converting it into immediately available energy when needed may help solve the impending energy crisis [2]. The steel industry, as a significant energy consumer, accounts for more than 8% of global energy usage [3,4]. Steel production is accompanied by substantial energy waste, particularly in the form of various gases that carry away a significant amount of energy [5,6]. Among these gases, blast furnace gas (BFG) is often directly emitted into the atmosphere or combusted, resulting in over 70% of the steel industry's CO_2 emissions [7]. Therefore, the recovery of BFG is crucial for CO_2 reduction and is expected to contribute to the achievement of carbon neutrality. In addition its waste heat utilization alleviates energy constraints and develops renewable energy sources [8].

As a byproduct of steel production, BFG possesses a high yield but low calorific value, making it a potentially valuable renewable energy source [9]. Various methods for harnessing BFG have been developed worldwide. For example, BFG can be mixed with high-calorific-value natural gas or coke oven gas (COG) and used directly for power generation by heating blast furnaces or boilers in power plants. BFG contains valuable components, and Kong et al. [10] attempted to produce hydrogen from BFG while verifying the feasibility and optimizing parameters using the ASPEN Plus software. Yong et al. [11] utilized Cu(I) as a catalyst to extract CO from BFG at room temperature, thus avoiding the need for high-temperature treatment. BFG can also be utilized for the production of other chemical substances. Porter et al. [12] employed a CCUS system to synthesize methanol, using BFG as a crucial raw material, with a CO_2 recovery rate of 80% achieved in the experiments. Lukashuk et al. [13] and colleagues proposed an iron-based catalyst that enables the conversion of BFG to hydrogen under high-temperature conditions.

However, existing studies on BFG reutilization are still in the laboratory stage and have not yet achieved industrial-scale implementation, but are expected to be applied in practice [14]. On the other hand, there have been attempts to directly generate electricity using BFG, showing promising progress within the industry. However, the production of BFG

* Corresponding author.
E-mail address: zhouhao@zju.edu.cn (H. Zhou).

https://doi.org/10.1016/j.energy.2023.128740
Received 30 March 2023; Received in revised form 16 July 2023; Accepted 10 August 2023
Available online 11 August 2023

is continuous, while electricity demand experiences peaks and valleys. Direct storage of BFG poses significant industrial land requirements and associated risks. Therefore, the development and utilization of a high-energy-density thermal energy storage (TES) device are urgently needed to match the supply and demand. The molten salt furnace heat storage system collects the BFG that cannot be used for power generation, reduces the waste of carbon energy, makes full use of its chemical energy, and stores it in high-temperature molten salt. In addition, it discharges electricity at peak times, which improves the utilization of carbon energy. The advancement and utilization of such TES devices hold the potential to bring substantial economic benefits to steel enterprises while alleviating carbon emission pressures.

TES is a key factor in improving the thermal energy utilization efficiency of various sectors of the economy, and TES in various industries is beneficial to the development of energy-saving technologies [15]. TES technology solves the conflict between energy and demand and contributes to the conservation and efficient utilization of energy [16]. Molten salt (MS) mixture (40% KNO_3, 60% $NaNO_3$, wt.%) has been selected for TES in solar applications due to the advantages of highest thermal stability, high freezing point (about 220 °C), and maximum allowable temperature limit (600 °C) [17–19]. Its become an ideal energy transfer and storage medium for solar power generation, grid peaking, effective utilization of waste wind energy, and site thermal energy recovery [2].

As research on TES methods and heat storage and transfer media deepens, storing excess energy in storage media through the design of TES devices has great potential and value, especially in studying the thermal characteristics of MS storage devices. TES in molten salt furnaces (MSF) and solar energy storage in MS using concentrating solar absorbers are currently suitable TES technologies [20,21]. Many articles have introduced the mechanical performance and the optimization performance of the TES. Currently, the research methods mainly involve numerical simulation combined with experimental studies. Wang [22] used a numerical method combining Monte Carlo ray tracing and finite volume methods to evaluate the photothermal coupling performance of finned MS receivers. The accuracy of the numerical model was verified by experimental data. Zou [23,24] used ANSYS Fluent software and ESS software to simulate the effects of aperture, inner diameter, and cavity length on the thermal performance of a helical coil. Zhou [25–27] et al. conducted research on laboratory-scale MS receivers using commercial CFD software and internal codes and applied them to a 600 MWh receiver to explore the thermal performance of the receiver.

Accurate and efficient models are crucial for designing and evaluating the thermal performance of TES systems, and many researchers have made significant efforts in model development [28]. Yu [29] established a comprehensive model for MS receivers using the multi-sectional lumped parameter method and analyzed the impact of critical parameters on the receiver system performance. Rodríguez-Sánchez M [30] et al. developed two simplified two-dimensional implicit scheme models to analyze the influence of mass flow rate and wind speed on the performance of the receiver under steady-state conditions and compared the results with ANSYS Fluent simulation results. Both simplified models could predict heat flux and tube wall temperatures with an error of less than 6%. Fritsch [31] et al. analyzed the applicability of different simplified FEM models for simulating the thermal performance of a single absorber tube. The results showed that FEM models with one-dimensional fluid units and constant heat transfer coefficients showed good consistency with detailed CFD models. The FEM model is verified using measurement data from the Solar Two receiver. Albarbar [32] et al. established a thermal model for a 20 MW external receiver using MATLAB and SIMULINK. They conducted a detailed study of the effect of the receiver tube parameters on the receiver performance. Xu [33] developed a transient numerical model for non-steady-state thermal analysis of a solar external receiver and solved it using numerical integration. They calculated the temperature change rate with time, as well as the variation of thermal properties of the receiver tube and heat transfer fluid with temperature.

Research on heat transfer in water/steam and MS in heat exchangers has also been conducted [34]. Huang [35] conducted experimental research on the heat transfer performance of a spiral tube MS steam generator and comprehensively studied its wall temperature distribution, steam production rate, and thermal efficiency. However, little research has been done on the heating process of the MSF. Ning [36] used computational fluid dynamics (CFD) technology to address this gap to establish a numerical model of the MSF. The model considers the gas flow, combustion, and radiative heat transfer in the furnace to optimize the MSF performance. However, the study did not comprehensively analyze the heat storage performance of the MSF.

In recent years, the application of molten salt thermal storage systems (MSTES) has gained significant attention and success in the field of concentrated solar power (CSP) [37]. The commercial operation of such systems has demonstrated their effectiveness in storing and utilizing thermal energy [38]. However, the potential of applying MSTES to recover and harness the waste heat from BFG in the steel industry remains largely unexplored. Previous research in this field has predominantly focused on the thermal performance analysis of solar absorbers, while the investigation of heat transfer in combustion-heated MSF has received limited attention.

Moreover, it is crucial to consider the dynamic nature of the heating process in MSF. The non-steady-state heat conduction and radiation involved in the heating process pose additional challenges that require comprehensive research and understanding [39]. Currently, the knowledge and understanding of these phenomena are still in the early stages, and further studies are needed to fully comprehend and optimize the performance of MSF. This paper presents an innovative approach to studying thermal energy storage using a 1.05 MW MSF under non-uniform heat flow conditions. Transient numerical models were established using ANSYS FLUENT and MATLAB 2021a software to analyze further the MSF thermal performance under different heating conditions. Through the mutual verification of numerical simulations and experimental data from the 1.05 MW MSF experimental bench, this study seeks to better understand the heating process of MSF and to analyze the temperature distribution and transient changes of the MS and the coil during the heating process. This rare work guided the on-site heat storage process of MSF to support the recovery and utilization of waste heat from BFG.

2. Experimental system and setup

2.1. MSF experimental system

Fig. 1 shows the MSF heat storage experimental system, which can be divided into three parts: MS energy storage system, heating system, and information control and acquisition system. The MS storage system is to pump the low-temperature MS from the molten salt cold tank into the coil through the molten salt pump, which is heated by the high-temperature coils to high-temperature MS and then stored in the molten salt hot tank. The MSF heats the coils by burning diesel fuel from the oil tank through the diesel burner. The information control collection system collects information from the thermocouples and flow meters installed in the experimental system and regulates the experimental system based on this information. The detailed dimensional information of the experimental system is listed in Table 1. Thermocouples are placed on the outer wall of the coil, the MS outlet, the MS inlet, the flue gas outlet and above the furnace chamber. Among them, the thermocouple on the outer coil wall is a measurement point arranged every 8 layers in the vertical direction. A total of 10 measurement points are set up (the specific location is shown in Fig. 2). The mass and volume flow meters are installed at the MS inlet and the diesel burner inlet, respectively.

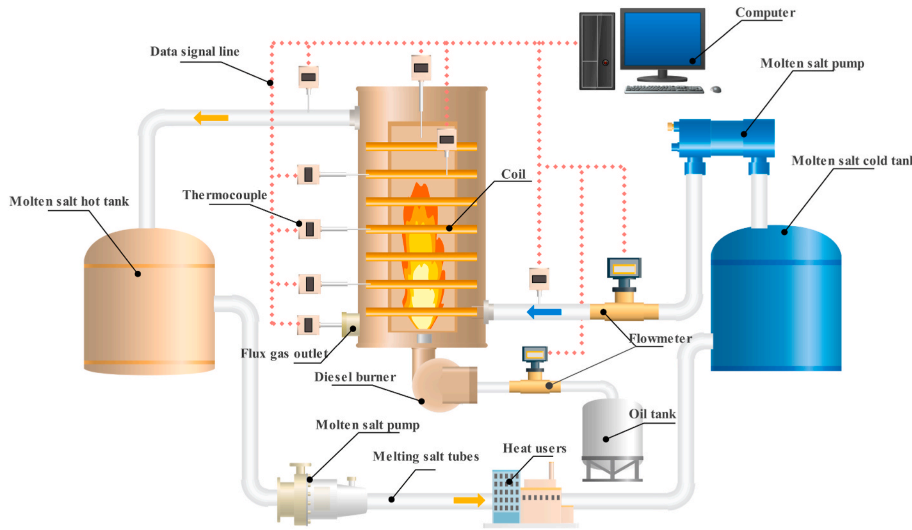

Fig. 1. MSF heat storage system.

Table 1
The detailed dimensional information of the experimental system.

	Parts	Parameter	Value	Unit
MSF	Furnace body	Furnace shell height	3602.00	mm
		Furnace shell diameter	1364.00	mm
	Coils	Coil inner diameter	30.00	mm
		Coil outer diameter	38.00	mm
		Coil length	314.16	m
		Coil pitch	38.00	mm
		Coil curvature radius	625.00	mm
	Flue	Flue cross-sectional area	0.32	m^2
		Total flue gas outlet cross-sectional area	0.0874	m^2
	Burners	Burner diameter	456.00	mm
		Air inlet area	0.0287	m^2
		Guide vane angle	45°	–
		Heat absorption area of	19.00	m^2
		Rated heat supply	1.05	MW
Material	Fuel	Diesel density (30 °C)	0.84	g/ml
		Diesel calorific value	42652.00	kJ/kg
		Diesel rated consumption	9.54	kg/h
	Air	Air Density (30 °C)	1.293	kg/m^3
		Air-fuel ratio	14.82	–
	Steel	Thermal conductivity of steel	23.60	$W/m^2\cdot°C$

2.2. Experimental setup

During the experiment, the molten salt temperature (ST) in the MS cold tank is first checked to reach the required inlet temperature. The diesel burner is ignited and the coil is preheated uniformly using a low heating load. After all coil layers are above 290 °C, the low-temperature MS in the MS cold tank is pumped into the coil at the experimentally set mass flow rate while the diesel burner is switched to the experimentally required heating load. The MS is heated in the high-temperature coil and stored in the MS hot tank through the outlet on the upper side of the furnace, during which the coil wall temperature (WT), the molten salt inlet temperature (ST-inlet), the molten salt outlet temperature (ST-outlet), the molten salt inlet mass flow rate (SR-inlet) and the diesel flow rate are recorded.

2.3. Laboratory-scale MSF

The MSF is a combination of a burner and a heat exchanger, whose primary purpose is to transfer the heat of combustion to MS by convection and radiation. In Fig. 2(a), the main body of the heat storage system built in this paper is a double-loop vertical MSF experimental platform consisting of two main parts: the furnace body and the combustion system. The structure of the MSF is coil-type, and the furnace body is composed of heating coils and a shell. The heating coil is densely coiled along the furnace body using the same diameter steel pipes. The MS of the spiral tube constantly changes direction in its forward motion, thus causing a secondary circulation in the cross-section and intensifying heat transfer.

Fig. 2(b) presents the MSF geometric model and the 3D cutaway view of the bottom. The burner is located at the MSF bottom, and diesel fuel combustion generates high-temperature radiation and flue gas. An annular flue gas return chamber is left between the coil and the shell of the MSF, and the coil is arranged densely as a “partition wall” to take full advantage of the heat. The coil wall controls the flow direction of the high-temperature flue gas so that it rises to the top of the furnace and can be discharged from the flue gas outlet through the flue gas return chamber.

The main role of the burner is to generate radiant heat flow and high temperature flue gas to provide the heat source for the MSF. Due to the complex and dangerous composition of BFG, there is no BFG available in the laboratory that can meet the entire experimental requirements. The main objective of this study is to analyze and test the thermal storage

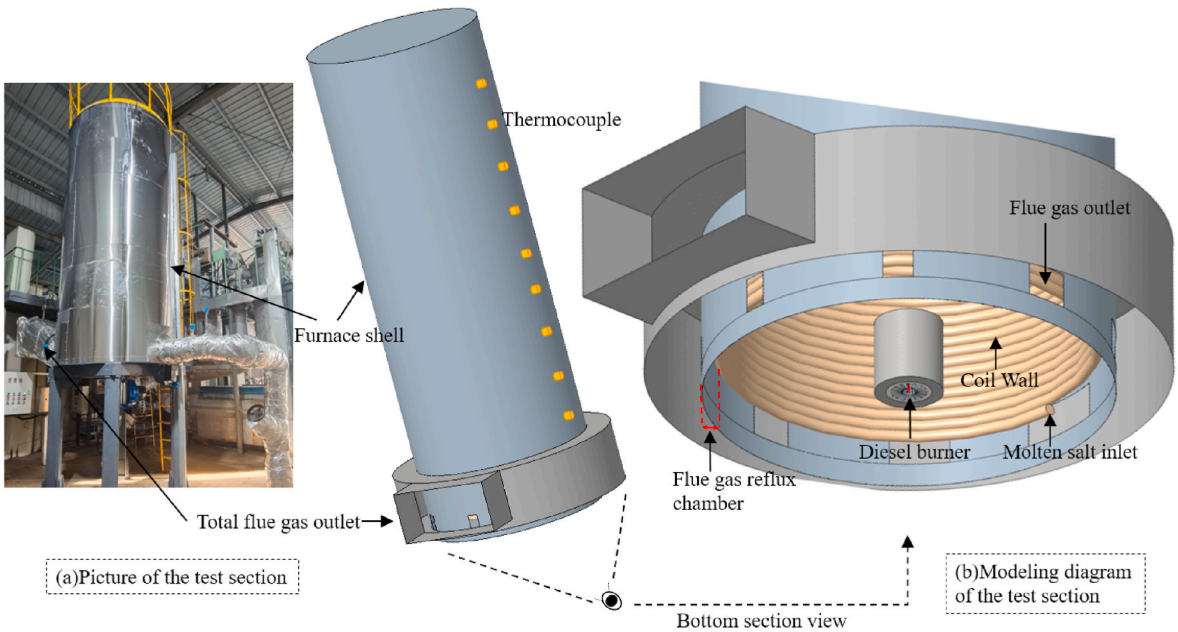

Fig. 2. MSF structure.

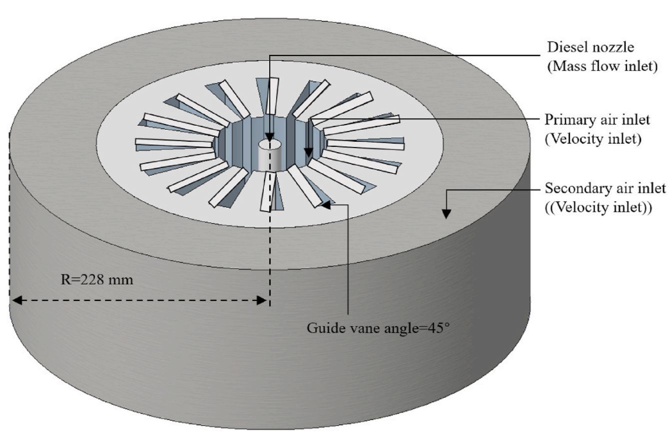

Fig. 3. Burner structure.

performance of the MSF by experimentally verifying the developed program code. The choice of fuel will not have an impact on this work, so diesel fuel was used instead of BFG as a fuel for the laboratory scale MSF for the experiments.

The principle of the air and fuel injection system of the burner is introduced in Fig. 3. The burner has a radius of 228 mm, and the diesel nozzle is located in the center of the burner for fuel injection (diesel spray). The primary air enters through 16 guide vanes (angle is 45°) around the nozzle to keep the fuel steadily on fire and burning, and to avoid thermal decomposition by direct injection into the high-temperature flue gas reflux zone. The secondary air enters through the annular holes around the burner to provide air for the fuel combustion completely.

2.4. *MS physical properties*

The MS flowing in the MSF is the most widely used solar salt [40,41]. The physical properties of the MS can be calculated according to the formula in Table 2.

3. Numerical modeling

Fig. 2 illustrates the structure of the MSF, a thick insulation material is employed in the furnace shell to minimize heat loss and achieve optimal adiabatic conditions. This prevented us from testing the radiation flux distribution inside the furnace chamber utilizing an external device. Due to the limited availability of experimental data, numerical simulation using ANSYS FLUENT 16.0, and MATLAB R2021a are conducted to investigate the MSF thermal performance. The outer wall surface of the coil toward the fire (FW) is selected as the main simulation object in FLUENT. The obtained heat flux distribution is then inputted into the MATLAB program developed in this study as the thermal boundary condition to simulate and analyze the MSF thermal performance.

3.1. *FLUENT computational model and mesh division*

The governing equations of the FLUENT simulation are as follows.

3.1.1. *Main governing equations*

Continuity equation

Table 2
Solar salt physical properties [42].

Parameter	Symbol	Value	Unit	Formulas
Temperature	T	290	°C	–
Density	ρ	1906	kg/m^3	2090–0.636 × T
Specific heat	C_p	1493	J/(kg·°C)	1443 + 0.172 × T
Thermal conductivity	λ	0.4984	W/(m·°C)	0.4433 + 0.19 × 10^{-4} × T
Thermal diffusivity	α	1.75 × 10^{-7}	m^2/s	1.410 × 10^{-7}+1.157 × $10^{-10}T$
Dynamic viscosity	μ	0.0035	Pa·s	(22.714–0.120× T+2.281 × 10^{-4} × T^2-1.474 × 10^{-7} × T^3) × 10^{-3}

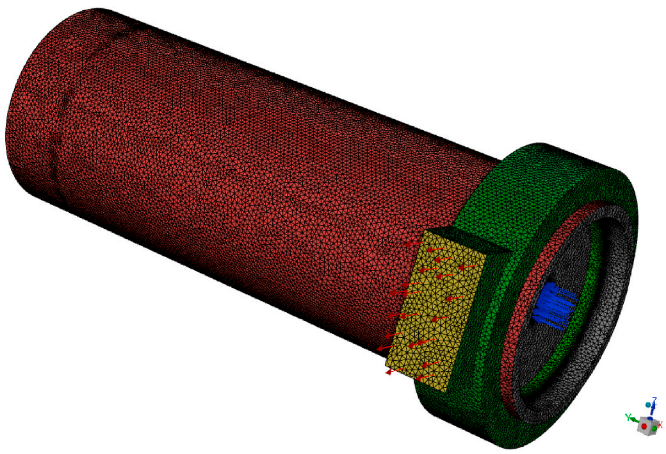

Fig. 4. Computational mesh of the MSF.

$$\frac{\partial(\rho u)}{\partial x}+\frac{\partial(\rho v)}{\partial y}+\frac{\partial(\rho w)}{\partial z}=0 \tag{1}$$

Mass conservation equation

$$\frac{\partial(\rho u_i)}{\partial x_i}=0 \tag{2}$$

Momentum equation

$$\frac{\partial(\rho u_i u_j)}{\partial x_i}=-\frac{\partial p}{\partial x_i}+\frac{\partial}{\partial x_j}\left[(\mu_t+\mu)\left(\frac{\partial u_i}{\partial x_j}+\frac{\partial u_j}{\partial x_i}-\frac{2}{3}\frac{\partial u_l}{\partial x_l}\delta_{ij}\right)\right]+\rho g_i \tag{3}$$

Energy equation

$$\frac{\partial(\rho u_i h)}{\partial x_i}=\frac{\partial}{\partial x_i}\left[c_p\left(\frac{\mu}{\mathrm{Pr}^2}+\frac{\mu_t}{\mathrm{Pr}_t}\right)\frac{\partial T}{\partial x_i}\right] \tag{4}$$

3.1.2. Turbulence equations

The swirling burner results in a relatively high Reynolds number of the mixed fluid in the furnace. Due to the greater accuracy of the Realizable k-ε turbulence model over the k-ω turbulence model under high Reynolds number conditions, it is employed to simulate the combustion of the fuel and the flow and heat transfer of the high-temperature flue gas within the MSF [43,44].

K and ε equation

$$\frac{\partial(\rho u_i k)}{\partial x_i}=-\frac{\partial}{\partial x_i}\left[\left(\mu+\frac{\mu_t}{\sigma_k}\right)\frac{\partial k}{\partial x_j}\right]+G_k+G_b-\rho\varepsilon \tag{5}$$

$$\frac{\partial(\rho u_i \varepsilon)}{\partial x_i}=-\frac{\partial}{\partial x_i}\left[\left(\mu+\frac{\mu_i}{\sigma_\varepsilon}\right)\frac{\partial \varepsilon}{\partial x_j}\right]+C_1\frac{\varepsilon}{k}(G_k+C_3G_b)-C_2\rho\frac{\varepsilon_2}{k} \tag{6}$$

The turbulent viscosity μ_t is calculated from the following equation:

$$\begin{aligned}\mu_t&=c_\mu\rho\frac{k^2}{\varepsilon},\\ G_k&=\mu_t\frac{\partial u_i}{\partial x_j}\left(\frac{\partial u_i}{\partial x_j}+\frac{\partial u_j}{\partial x_i}\right),\\ G_b&=\beta g_i\frac{\mu_t}{Pr_t}\frac{\partial T}{\partial x_i}\end{aligned} \tag{7}$$

where $C_1=1.44$, $C_2=1.92$, $C_\mu=0.09$, $\sigma_k=1.0$, $\sigma_\varepsilon=1.3$, and $C_3=\tanh(|v_p/v_n|)$, where v_p and v_n are the components of the fluid velocity vector.

3.1.3. Species transport equation

The diesel combustion is modeled using the mixture fraction-probability density function (PDF) formulation [45,46].

$$\frac{\partial}{\partial x_j}(\rho u_j\bar{f})=\frac{\partial}{\partial x_j}\left(\Gamma_{e,f}\frac{\partial\bar{f}}{\partial x_j}\right) \tag{8}$$

3.1.4. Radiation model

Due to the significant radiation and high-temperature flue gas generated by fuel combustion, calculating the radiation heat transfer between the furnace flame and the coil wall is particularly important. The Discrete-Ordinates Method (DO) [47] can model semitransparent materials and non-gray bodies as gray bodies in any radiation band, and its suitable optical thickness is comprehensive. Therefore, the DO model is selected to calculate the radiation [30,48].

$$\begin{aligned}&\overrightarrow{\nabla}\cdot(I_\lambda(\overrightarrow{r},\overrightarrow{s})\overrightarrow{s})+(a_\lambda+a_s)I_\lambda(\overrightarrow{r},\overrightarrow{s})=a_\lambda n^2 I_{b\lambda}\\ &\quad+\frac{a_s}{4\pi}\int_0^{4\pi}I_\lambda(\overrightarrow{r},\overrightarrow{s})\Phi(\overrightarrow{s}\cdot\overrightarrow{s}')d\Omega'\end{aligned} \tag{9}$$

$$I_\lambda(\overrightarrow{r},\overrightarrow{s})=\sum_k I_{\lambda k}(\overrightarrow{r},\overrightarrow{s})\Delta\lambda_k \tag{10}$$

$$E_b(\lambda,T)=(F(0\to n\lambda_2T)-F(0\to n\lambda_1T))n^2\frac{\sigma T^4}{\pi} \tag{11}$$

Eq. (9) expresses the radiative transfer equation for spectral intensity $I_\lambda(\overrightarrow{r},\overrightarrow{s})$, where λ is the wavelength, $\overrightarrow{s}$ is the scattering direction vector, α_s is the scattering coefficient, α_λ is the spectral absorption coefficient, n is the refractive index, Φ is the phase function, and Ω is the solid angle. $I_{b\lambda}$ is the blackbody intensity calculated using the Planck function. Eq. (10) sums the entire wavelength band to calculate the total intensity in the direction $\overrightarrow{s}$ at position $\overrightarrow{r}$. Eq. (11) is used to calculate the blackbody radiation intensity $I_\lambda(\overrightarrow{r},\overrightarrow{s})$ per unit solid angle in each wavelength band. Here, $F(0\to n\lambda T)$ represents the energy radiated by a blackbody at temperature T in the wavelength range from 0 to λ, emitted from a medium with refractive index n, and λ_1 and λ_2 are the wavelength boundaries of each band.

3.1.5. Mesh division and boundary conditions

Fig. 4 shows the computational mesh of the MSF. Due to the large size difference between the MSF body and coils, the unstructured grid

Table 3
Boundary conditions.

Boundary	Boundary conditions	Value			
		25%	50%	75%	100%
Primary air inlet	Velocity inlet	$V=1.96$ m/s, $T=673$ K	$V=3.91$ m/s, $T=673$ K	$V=5.87$ m/s, $T=673$ K	$V=7.82$ m/s, $T=673$ K
Secondary air inlet	Velocity inlet	$V=2.94$ m/s, $T==673$ K	$V=5.89$ m/s, $T==673$ K	$V=8.83$ m/s, $T==673$ K	$V=11.78$ m/s, $T==673$ K
Diesel oil inlet	Mass flow inlet	0.00728 kg/s, T = 300 K	0.14563 kg/s, T = 300 K	0.02185 kg/s, T = 300 K	0.02913 kg/s, T = 300 K
Flue gas outlet	Pressure outlet	−20 Pa	−20 Pa	−20 Pa	−20 Pa
Diesel injection speed	From Discrete Phase Models	40 m/s	40 m/s	40 m/s	40 m/s
Burner cone nozzle angle	From Discrete Phase Models	60°	60°	60°	60°

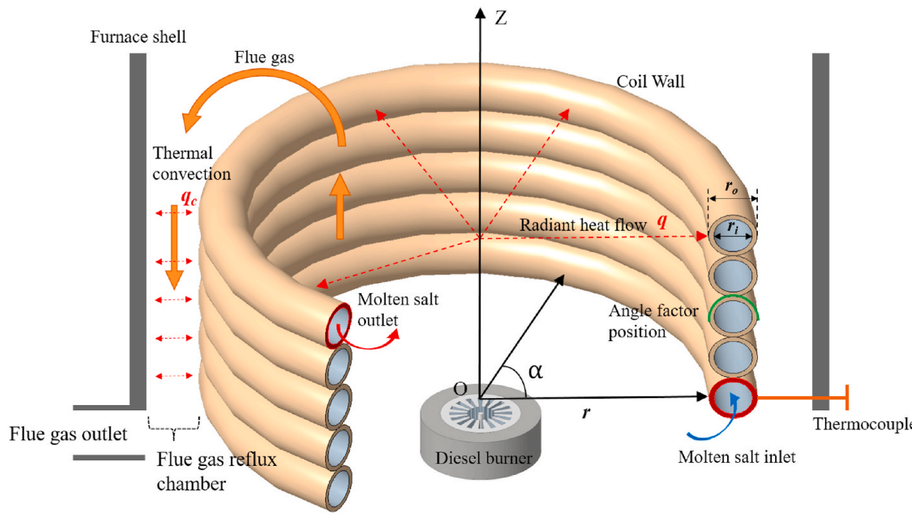

Fig. 5. Computational domain of the MSF.

divides the furnace body. The structured O-grid is used to mesh the coil individually and encrypt the coil wall surface.

The inlet of the coil is designated as the velocity inlet, the outlet of the coil is designated as the pressure outlet and the furnace shell is assumed to be an adiabatic wall. The heat exchange between different coils is ignored. The diesel nozzle is a conical nozzle with an angle of 60°, the primary and secondary air is the velocity inlet, the nozzle fuel inlet is the mass inlet, and the flue gas outlet is the pressure outlet. Table 3 explains the boundary conditions.

3.2. MATLAB computational model and mesh division

The closed nature of the MSF experimental equipment leads to minimal experimental data that can be measured during the experiments, which leads to a lack of generality of the experimental data. Numerical modeling assists in solving this problem and saves experimental costs. The calculated heat flux density distribution of the FW is used as the thermal boundary conditions for the MATLAB 2021a calculation model.

The coil absorbs and converts radiant heat from the diesel combustion into the thermal energy of the internal MS. In operation, diesel combustion is easily affected by other factors, so the temperature distribution on the coil surface often keeps in a non-steady state. The transient numerical simulation [49] of the coil heating process is conducted to investigate the transient MSF thermal performance.

3.2.1. Computational domain division

Fig. 5 briefly summarizes the computational domain of the MSF. A combination of heat radiation from the combustion and heat convection from the high-temperature flue gas heats the MS in the coil. The radiation occurs between the furnace flame and the FW. Convection occurs mainly in the flue gas return chamber between the coil and the furnace shell, with a portion of convective heat transfer in the furnace chamber as well. With the center of the burner (O) as the origin, the coil is wound into a circle with a radius (r) of 60 6 mm, along the vertical upward direction (Z-axis); the outer diameter (r_o) of the coil is 38 mm and the inner diameter (r_i) is 30 mm. The MS enters through the inlet, is heated by radiant heat flow (q) and convective heat (q_c), and exits through the outlet. The position of the coil and the MS is determined by the method of polar coordinates. The heat absorbed on the coil wall is diffused in three dimensions.

3.2.2. Mesh division

According to heat transfer principles, the absorbed heat in the coil walls diffuses in three-dimensional space and spreads along the coil by thermal conduction. The FW is influenced by natural and forced convection. The outer wall of the coil radiates energy to the surroundings because it absorbs the heat emitted by the flame and the temperature

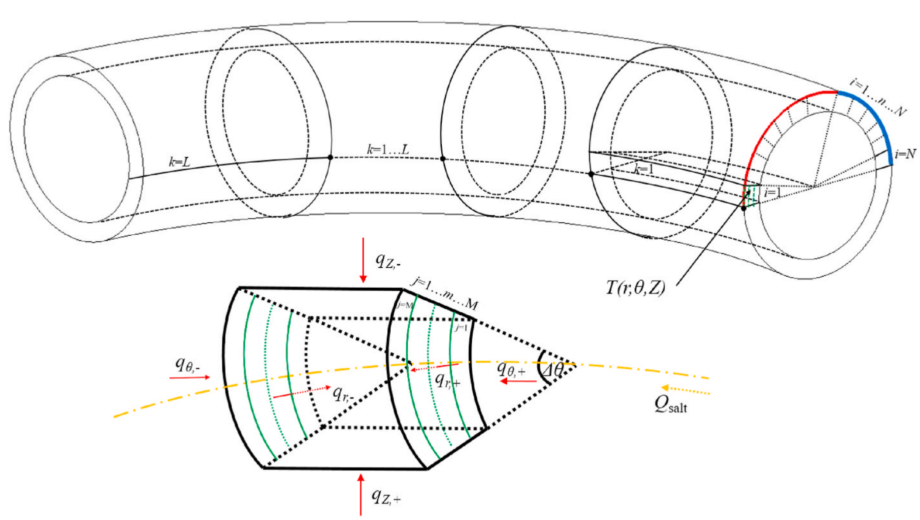

Fig. 6. Coil discretization and inflow heat flux density of the control unit.

becomes very high. The coil must first be discretized to calculate the transient temperature distribution of the coil and the MS. Due to the large numerical values of the heat flux density on the FW and the relatively small variation of the heat flux density on adjacent coils, it can be assumed that there is no axial heat exchange in the coils. However, there is a significant temperature difference in the coil cross-section, and the radiation heat transfer outside the coil is much more pronounced than the convective heat transfer inside the coil.

To calculate the transient temperature of the coil and the MS, as shown in Fig. 6, the coil needs to be discretized first. The coil consists of 80 layers, and each layer is calculated separately for simplicity in modeling. Each coil layer is divided into L parts (L = 78) along the circumferential direction, and the coil has 80L parts. Thus, the MS must pass through 6240 parts from the inlet to the coil outlet. Since the diameter of each layer is very small compared to the height of the coil wall, the temperature distribution of the cross-section of every layer is approximated to be symmetrical in the up-down direction along the direction of incident radiation. Therefore, only half of the circular arc of the coil layer needs to be considered in the modeling. The half-circular arc of the coil is divided into N sections (N = 40), starting from the side facing the flame and numbered clockwise as 1, 2, …, n, …, N, where the first section corresponds to the projection of the incident radiation. The coil layer is divided into M parts (M = 4) along the radial direction from the inside to the outside. The axial coil segment is named the kth segment along the MS flow direction, where the (j-1) × L+1 segment is the inlet and the j × L segment is the outlet, and j is the index of the coil layer from bottom to top, with values from 1 to 80. After discretization, any unit on the coil can be represented by its coordinates (m, n, k). To display the directions of m, n, and k, $T(r, \theta, Z)$ is used instead of $T(m, n, k)$ to represent the temperature in any unit, where r represents the radial direction, θ represents the circumferential direction and Z represents the axial direction.

3.2.3. Heat transfer analysis

As shown above, According to the law of conservation of energy, the sum of energy is equal to the sum of the increase in unit thermal energy per unit time $\Delta\tau$. The non-boundary units are influenced by the surrounding 6 units, and there are two heat flows in each direction of radial, circumferential, and axial directions. Therefore, the following Eq. (12) can be obtained.

$$q_{r,+} + q_{r,-} + q_{\theta,+} + q_{\theta,-} + q_{Z,+} + q_{Z,-} = \rho c_p \Delta V \frac{\Delta T}{\Delta \tau} \tag{12}$$

The heat flow is calculated using Eq. (13). The antecedent coefficient of temperature difference is K ($K = 1/R$). The circumferential and axial coefficients are expressed by Eq. (14) and Eq. (15) respectively.

$$q = \frac{1}{R}\Delta T \tag{13}$$

$$K_{\theta^-} = K_{\theta^+} = \frac{\lambda \Delta r \Delta Z}{r\Delta\theta} \tag{14}$$

$$K_{Z^-} = K_{Z^+} = \frac{\lambda r \Delta r \Delta\theta}{\Delta Z} \tag{15}$$

The heat transfer of the radial unit is calculated by Eq. (16) [50]. The heat transfer of the radial unit can be defined as a one-dimensional radial thermal conductivity. The coil inner diameter coefficient and outer diameter coefficient are shown in Eqs. (17-18).

$$R = \Delta S \cdot r_{in} \cdot \ln(r_{out} r_{in}) / \lambda \tag{16}$$

$$K_{r^-} = \frac{\lambda \Delta\theta \Delta Z}{\ln\left(\frac{r}{r-\Delta r}\right)} \tag{17}$$

$$K_{r^+} = \frac{\lambda \Delta\theta \Delta Z}{\ln\left(\frac{r+\Delta r}{r}\right)} \tag{18}$$

The WT at non-boundary is calculated by the explicit difference Eq. (19), where i denotes the time series, and a is the thermal diffusivity [51].

$$\begin{aligned} T^{i+1}_{m,n,k} = {} & \frac{a\Delta\tau}{r\Delta r \ln\left(\frac{r}{r-\Delta r}\right)}\left(T^i_{m-1,n,k} - T^i_{m,n,k}\right) + \frac{a\Delta\tau}{r\Delta r \ln\left(\frac{r+\Delta r}{r}\right)}\left(T^i_{m+1,n,k} - T^i_{m,n,k}\right) + \frac{a\Delta\tau}{(r\Delta\theta)^2}\left(T^i_{m,n+1,k} + T^i_{m,n-1,k} - 2T^i_{m,n,k}\right) \\ & + \frac{a\Delta\tau}{(\Delta Z)^2}\left(T^i_{m,n,k+1} + T^i_{m,n,k-1} - 2T^i_{m,n,k}\right) + T^i_{m,n,k} \end{aligned} \tag{19}$$

The calculation units at the boundaries need to be discussed separately, where the inner and outer wall surfaces are essential calculation areas. The FW is losing heat through convection and thermal radiation while receiving the radiant heat flow from the flame. The flowing MS in contact with the inner wall surface of the coil carries away part of the heat flow.

$$\begin{aligned} & \left[\frac{\delta_{m,0}}{\varepsilon_0} - \left(\frac{1}{\varepsilon_0} - 1\right)F_{m,0}\right]\frac{q_0}{\sigma} + \sum_{N}^{j=1}\left[\frac{\delta_{m,j}}{\varepsilon_j} - \left(\frac{1}{\varepsilon_j} - 1\right)F_{m,j}\right]\frac{q_j}{\sigma} - \left[\delta_{m,N+1} - F_{m,N+1}\right]T^4_{N+1} = \left[\delta_{m,0} - F_{m,0}\right]T^4_0 \\ & + \sum_{N}^{j=1}\left[\delta_{m,j} - F_{m,j}\right]T^4_j - \left[\frac{\delta_{m,N+1}}{\varepsilon_{N+1}} - \left(\frac{1}{\varepsilon_{N+1}} - 1\right)F_{m,N+1}\right]\frac{q_{N+1}}{\sigma} - F_{m,0}\frac{q''_h}{\sigma}(1-\varepsilon) \end{aligned} \tag{20}$$

The heat flux density distribution has been obtained in the numerical calculation of FLUENT. The net heat flow method [52] calculates the net inflow of radiant heat flow $q^i_{M,n,k}$ for each cell in the circumferential direction using Eq. (20), where m = 0,1, …, N+1. The natural convection heat transfer coefficient $h_{n,air}$ was subsequently calculated by Eqs. (21-23).

$$Gr = \frac{g\Delta t l^3}{T_{amb} v^2} \tag{21}$$

$$Nu_{n,air} = 0.11(Gr \cdot Pr)^{1/3}_m \tag{22}$$

$$h_{n,air} = \frac{\lambda_{air} Nu_{n,air}}{l} \tag{23}$$

The high-temperature flue gas is discharged through the chamber between the coil and the furnace shell, and it exchanges heat with the outer wall surface of the coil reflux side (RW). The heat flow is transferred to the coil when the temperature of the RW is lower than the temperature of the high-temperature flue gas; conversely, forced convection losses occur on the RW. This process can be assumed as the flue gas flow outside the coil, and the heat transfer coefficient $h_{f,air}$ can be calculated by Eqs. (24-26). Therefore, the overall convection coefficient of the outer coil wall unit is $h_{total} = (H_{f,air}^{3.2} + H_{n,air}^{3.2})^{1/3.2}$ [53].

$$\mathrm{Re} = \frac{ud}{v} \tag{24}$$

$$Nu_{f,air} = 0.193\mathrm{Re}^{0.618}\,\mathrm{Pr}^{1/3} \tag{25}$$

$$h_{f,air} = \frac{\lambda_{air} Nu_{f,air}}{d} \tag{26}$$

The heat transfer from the center of the outermost unit to the internal environment is influenced by the thermal resistance of the coil and the thermal resistance of convective heat transfer. The temperature difference pre-coefficient of the two thermal resistances is Eq. (27).

$$K_{r,o} = \frac{\Delta Z}{\frac{1}{\lambda \Delta\theta}\ln\left(\frac{r_o}{r_M}\right) + \frac{1}{\Delta\theta r_o h_{total}}} \tag{27}$$

where r_o is the outer coil radius, and r_M is the radius of the outermost coil unit ($M = m$). From this, the explicit difference Eq. (28) can be calculated for the outermost cell of the outer wall.

$$\begin{aligned}&\frac{\lambda\Delta\theta\Delta Z}{\ln\left(\frac{r}{r-\Delta r}\right)}\left(T_{m-1,n,k}^{i} - T_{m,n,k}^{i}\right) + K_{r,o}\left(T_{amb} - T_{m,n,k}^{i}\right) + \frac{\lambda \Delta r \Delta Z}{r\Delta\theta}\left(T_{m,n+1,k}^{i} + T_{m,n-1,k}^{i} - 2T_{m,n,k}^{i}\right) + \\ &\frac{\lambda r \Delta r \Delta\theta}{\Delta Z}\left(T_{m,n,k+1}^{i} + T_{m,n,k-1}^{i} - 2T_{m,n,k}^{i}\right) + \left(q_{L,m,k}^{i}\right)_{net}\cdot r_o\cdot\Delta\theta\cdot\Delta Z = \frac{c_p \rho r \Delta r \Delta\theta \Delta Z}{\Delta\tau}\left(T_{m,n,k}^{i+1} - T_{m,n,k}^{i}\right)\end{aligned} \tag{28}$$

Compared with the coil outer wall, the heat transfer of the calculation unit on the inner wall is simpler. Since the cells are small enough to assume a uniform temperature distribution of the MS cells, the

Table 4
Simulation cases.

case	Heating power of the MSF	Diesel volume flow rate	ST-inlet	SR-inlet
case1	25%	31.21 L/h	290 °C	1.7 kg/s
case2	50%	62.41 L/h	290 °C	1.7 kg/s
case3	**75%**	**93.62 L/h**	**290°C**	**1.7 kg/s**
case4	100%	124.83 L/h	290 °C	1.7 kg/s
case5	75%	93.62 L/h	260 °C	1.7 kg/s
case6	75%	93.62 L/h	320 °C	1.7 kg/s
case7	75%	93.62 L/h	350 °C	1.7 kg/s
case8	75%	93.62 L/h	380 °C	1.7 kg/s
case9	75%	93.62 L/h	290 °C	1.5 kg/s
case10	75%	93.62 L/h	290 °C	1.9 kg/s
case11	75%	93.62 L/h	290 °C	2.1 kg/s
case12	75%	93.62 L/h	290 °C	2.3 kg/s

convective heat transfer coefficient of the MS is calculated using the Gnielinski equation, as in Eq. (29-32).

$$Nu_f = \frac{(f/8)(\mathrm{Re}-1000)Pr_f}{1+12.7\sqrt{f/8}\left(Pr_f^{2/3}-1\right)}\left[1+\left(\frac{d}{l}\right)^{2/3}\right]c_t \tag{29}$$

$$c_t = \left(\frac{Pr_f}{Pr_w}\right)^{0.01} \tag{30}$$

$$f = \left(1.82\lg\mathrm{Re}_f - 1.64\right)^{-2} \tag{31}$$

$$h_f = \frac{\lambda_f Nu_f}{d} \tag{32}$$

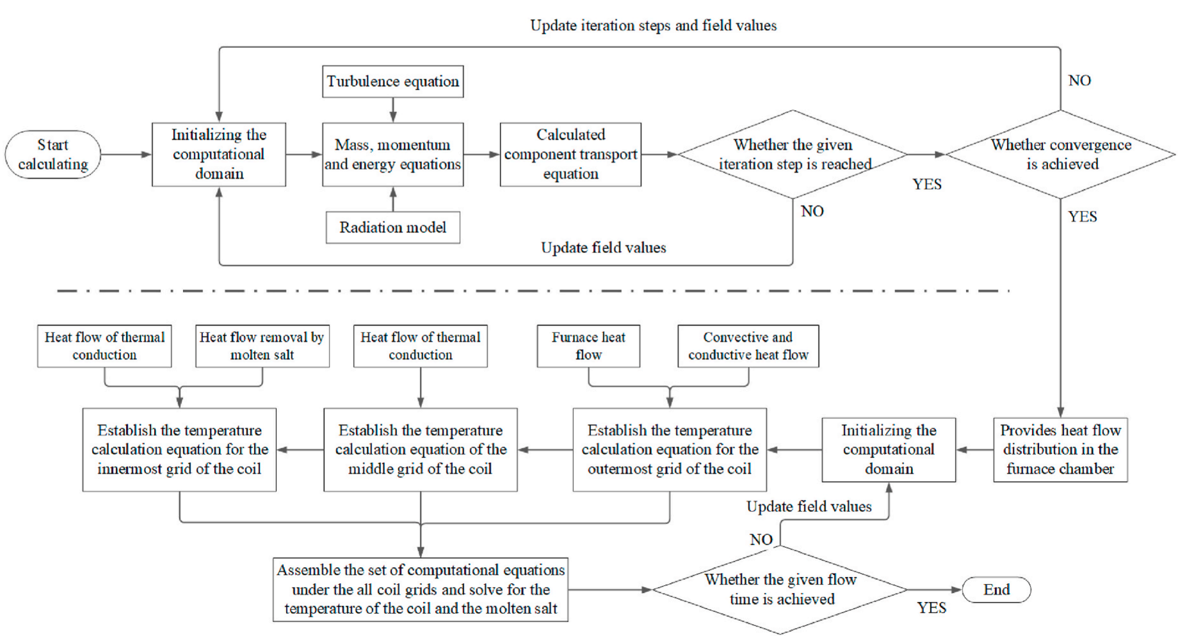

Fig. 7. Numerical simulation calculation process.

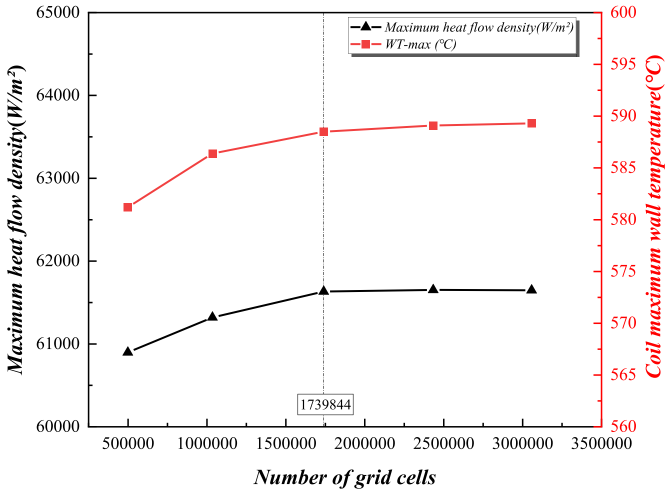

Fig. 8. Grid independence analysis.

Similar to calculating the outermost unit of the outer coil wall, the pre-coefficient $K_{1,n,k}$ can be inferred, as Eq. (33).

$$K_{1,n,k} = \frac{\Delta Z}{\frac{1}{\Delta\theta r_i h_i} + \frac{1}{\lambda\Delta\theta}\ln\left(\frac{r_1}{r_i}\right)} \tag{33}$$

where r_i is the inner radius of the coil and r_1 is the radius of the innermost unit ($m = 1$). The explicit difference Eq. (34) for the inner wall surface cell is derived.

It should be noted that some units will have a combination of both boundary conditions.

$$T^{i+1}_{m,n,k} = \frac{K_{1,n,k}\Delta\tau}{\rho c_p r\Delta r\Delta\theta\Delta Z}\left(T^i_{salt,k,b} - T^i_{m,n,k}\right) + \frac{a\Delta\tau}{r\Delta r\ln\left(\frac{r+\Delta r}{r}\right)}\left(T^i_{m+1,n,k} - T^i_{m,n,k}\right) + \frac{a\Delta\tau}{(r\Delta\theta)^2}\left(T^i_{m,n+1,k} + T^i_{m,n-1,k} - 2T^i_{m,n,k}\right) + \frac{a\Delta\tau}{(\Delta Z)^2}\left(T^i_{m,n,k+1} + T^i_{m,n,k-1} - 2T^i_{m,n,k}\right) + T^i_{m,n,k} \tag{34}$$

3.3. Numerical solution procedure

The numerical simulation is carried out as the explicit difference. The unit time is 0.005 s, and the Fourier number of the grid is less than 0.5, which is also in line with Bejan A [54] and Yang [55] et al. that the unit time should be minimal and the grid Fourier number should not exceed 0.5 to make the program converge.

In summary, the simulation of the heat flux density on the FW and the derivation of the driving equations for controlling each unit temperature on the coil has been presented in detail. Fig. 7 shows the specific steps of the simulation: (1) The heat flux density on the FW is calculated based on ANSYS FLUENT 16, during which the radiation model, the turbulence equation, and the component transport equation are considered. (2) When the calculation of heat flux density reaches convergence, it is output to MATLAB 2021a. (3) Initialize the coil calculation domain with the calculated heat flux density. (4) The temperature calculation equations for the outermost grid of the coil are developed, considering convective heat conduction and radiation (angular coefficient model is introduced). (5) The temperature calculation equations for the middle mesh of the coil are established considering heat transfer. (6) The temperature calculation equations for the innermost grid of the coil are formed, taking into account the MS convective heat transfer and thermal conductivity model. (7) The set of equations for the temperature calculating of all coil grids is constructed, and the WT and the ST are solved.

3.4. Case design

The experiments and simulations first determine the benchmark cases (case 3 in Table 4) The experimental data of case 3 are used to verify the reliability and performance of the numerical simulations and procedures. A total of 12 cases are simulated to discuss the MSF thermal performance by varying the heating power (heat flux density on the FW), the ST-inlet, and the SR-inlet. The rated heating load (100%) of the MSF is 1.05 MW, corresponding to a diesel combustion volume flow rate of 124.83 L/h. The details of all cases are summarized in Table 4.

4. Results and discussion

4.1. Grid independence analysis

A good grid is beneficial for obtaining accurate simulation results and saving computational resources. In Fig. 8, the grid independence analysis is performed by the maximum radiant heat flux density and the maximum wall temperature of the coil (WT-max) in the benchmark case. Grids with 498 766, 1 035 230, 1 739 844, 2 433 658, and 3 057 447 cells were selected to conduct the analysis. The number of cells in the grid increased by 39.88% from 1 739 844, the WT-max increased by only 0.1%, and the maximum radiant heat flux density increased by only 19.0 W/m^2, which is both much less than 1%. The grid is considered to have converged when the error gap between the compact grid and the relative grid is reduced to less than 1%. Therefore, the grid of 1739844 cells is finally selected for the subsequent study.

4.2. Heat flux distribution

The software FLUENT 16.0 is applied to simulate the heating process of the MSF using the selected grid to obtain the heat flux density distribution on FW. As shown in Fig. 9, with the heating power increase, the heat flux density gradually increases to about 70 kW/m^2 at the rated load. It is worth noting that when the heating power is low, the heat flux density on the FW is more evenly distributed due to the low flow rate of the diesel inlet and the low flame height. At the same heating power, the heat flux density gradually increases as the coil height rises. The heat flux density of the top coil is three times higher than the bottom coil at 75% load, and this value is greater at higher loads. The heat flux density received by the coil outer wall surface at the same height is uniform. Still, inevitable fluctuations can be caused by the flame combustion instability and the setting of the flue gas outlet. But it does not affect the data extraction and use of the MATLAB program next.

4.3. Model validation

The benchmark case of the MSF heat storage experiment is conducted to verify the performance and reliability of the model and procedure. The numerical simulations obtain the evolution of the WT and the ST inside the coil during the MS migration process. The simulated

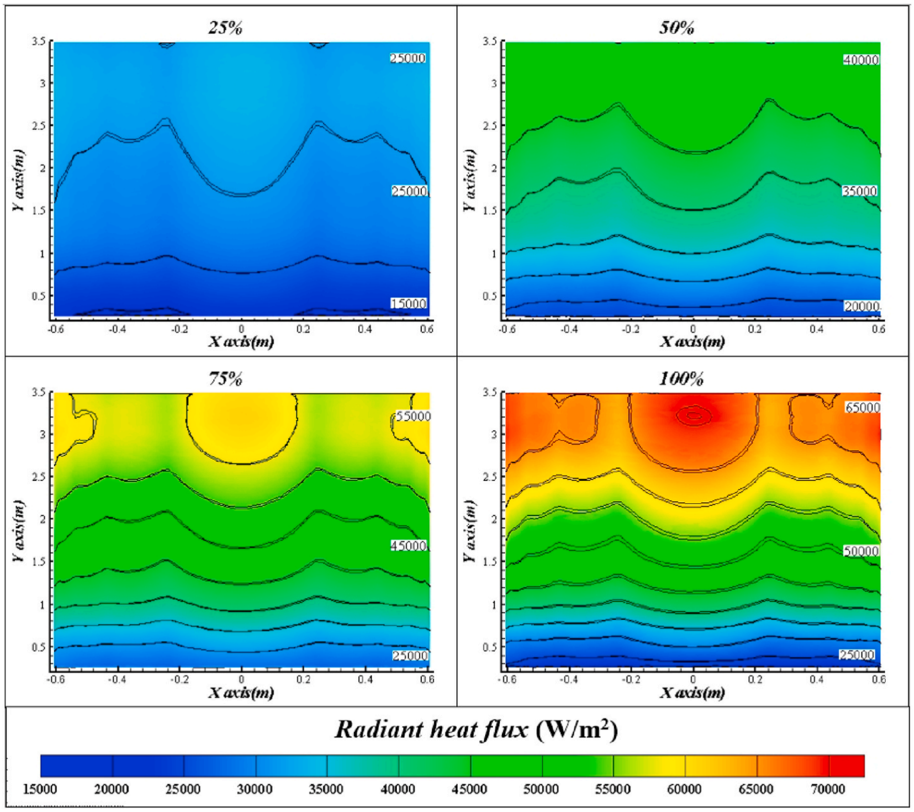

Fig. 9. Heat flux density distribution on the FW under different heating power.

results are compared with the experimentally collected ST-outlet and the temperature at 10 measurement points on the outer wall surface of the coil.

In Fig. 10, the temperatures of the 10 measurement points in the experiment match the temperatures of the corresponding points in the simulation with an average deviation of 2.90%. The temperature deviation at each point is less than 5% with a minimum temperature difference of 1.9 °C. In addition, the ST-outlet measured in the experiment is 566.5 °C, which is 13.92 °C higher than the simulated data, with a deviation of 2.46%. Therefore, it is considered that the model and underlying assumptions used to construct the computational procedure are valid and suitable for the thermal performance evaluation of the laboratory-scale MSF in this paper.

4.4. Transient thermal performance variation of the MSF

Before the operation, it is necessary to preheat the coil before adding the MS. If MS at around 290 °C is directly injected into the cold coil, it may solidify and block the coil. Therefore, this study conducted preheating simulations on the coil of the salt-cooled furnace. Under conditions where the temperature of the empty coil wall met experimental requirements, heat storage experiments and transient simulations are carried out for different operating conditions of the MSF.

First, the transient temperature distribution of the MS and the coil wall is obtained by discussing the simulation results of the 75% heating load case and 100% heating load case. Then three different experimental conditions are discussed separately, including the heating power (i.e., different heat flux densities on the FW), the ST-inlet and the SR-inlet, as shown in Table 4. Finally, the ST rise after heating by the coil and the transient ST at different times are displayed by analyzing the temperature change during the MS flow in the simulation. In addition, the inner wall temperature (WT-in) and the outer wall temperature (WT-out) of the coil can be obtained.

4.4.1. Identification and result of the benchmark case

Fig. 11 reveals the relationship between the WT-in and WT-out and ST at the coil cross-section $\theta = 0°$. The temperature trends are the same for the above two heating load cases. At 75% heating, WT-in and WT-out increase gradually with the MS migration route. The highest WT-out can reach 574.20 °C, and the ST can reach 552.58 °C. Both the WT-in and WT-out are higher than the ST, so the MS is gradually heated during the flow in the coil, and the heating rate is gradually slowed. When the heating load was increased to 100%, both WT-in and WT-out are increased with an average increase of about 10.50 °C. The highest WT-out can reach 582.84 °C, while the highest ST increases to 568.07 °C. By calculating the temperature difference between WT-in and WT-out and ST separately, the temperature difference decreases gradually with the

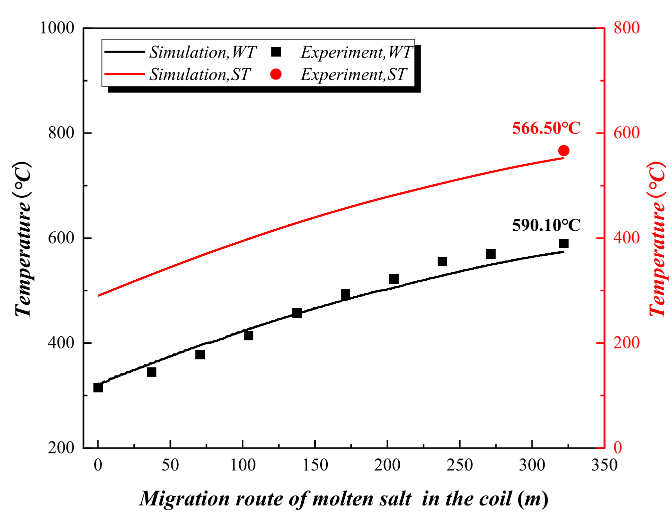

Fig. 10. Experimental data and model simulation validation.

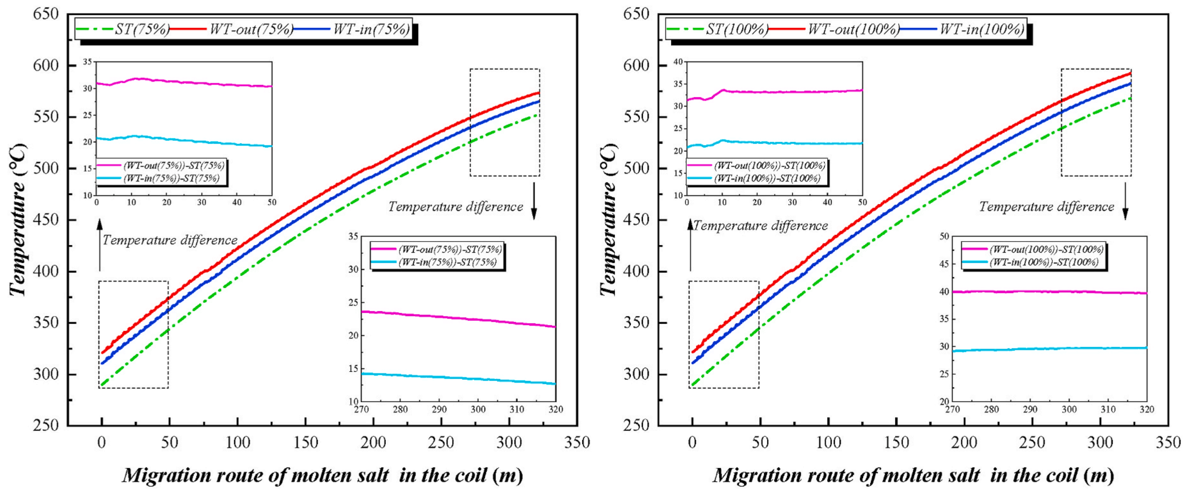

(a) 75% heating load (b) 100% heating load

Fig. 11. Trend of ST and WT-in and WT-out at coil cross-section $\theta = 0°$.

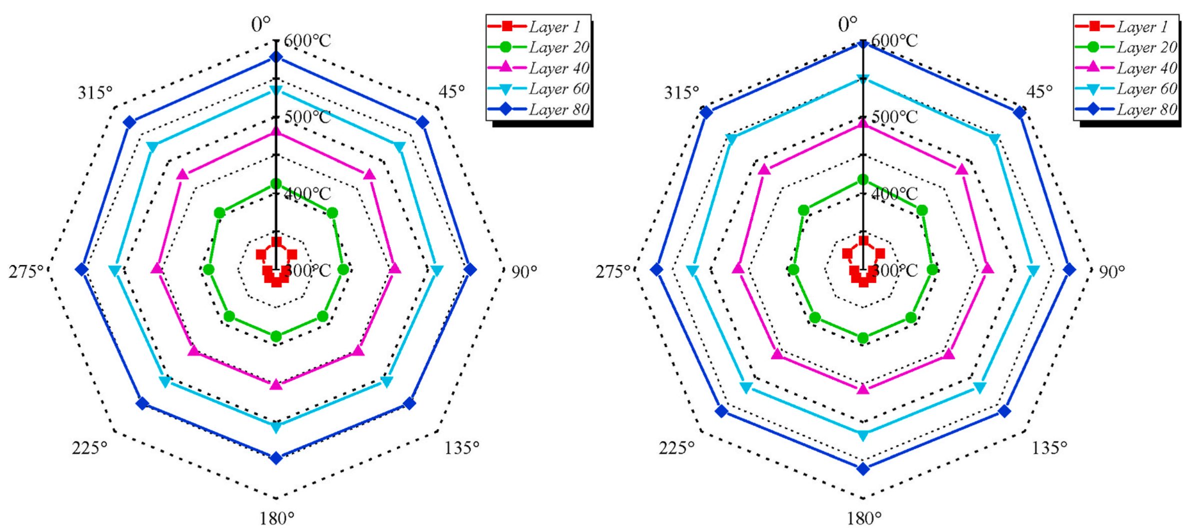

(a) 75% heating load (b) 100% heating load

Fig. 12. WT-out distribution on coil cross-section at different circumferential positions (0°, 45°, 90°, 135°, 180°).

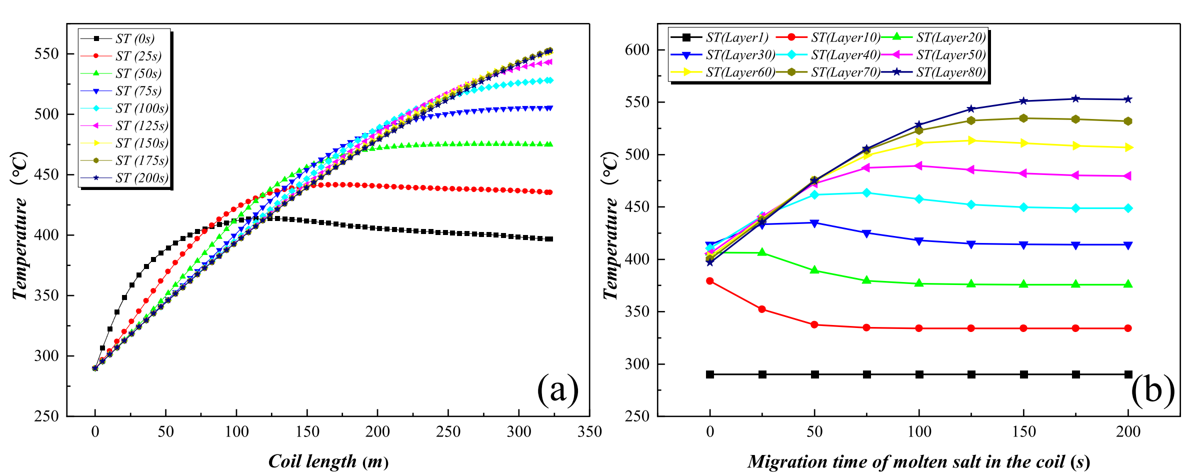

Fig. 13. Temperature distribution of the MS chamber at different times.

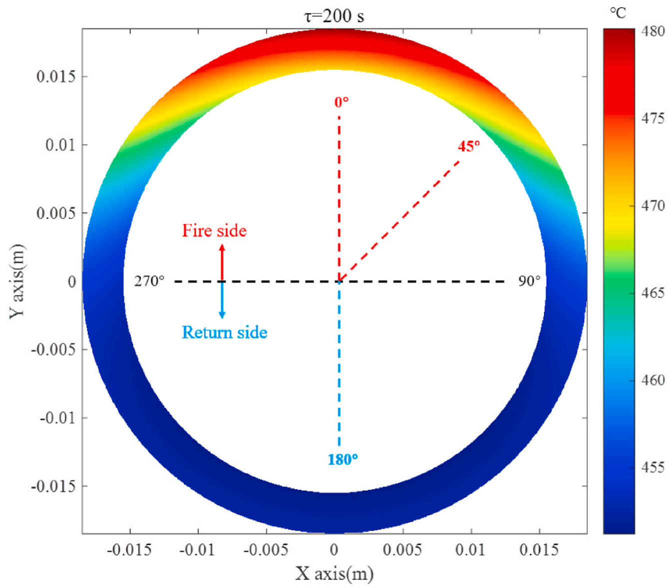

Fig. 14. Temperature distribution cloud diagram (40th layer coil cross-section).

MS flow in the 75% heating load case. In the first 50 m of the MS flow, the difference between the WT-out and the ST is kept above 30 °C, and the temperature difference is reduced to about 22.5 °C in the last 50 m, while the difference between the WT-in and the ST is only about 13 °C. The goal of the MSF heat storage is to output MS above 550 °C. If the temperature difference between the corresponding WT and ST is smaller at this point, then the safer the coils are subjected to, proving that the heating is more efficient. Comparing the 75% heating load case with the 100% heating load case, it can be seen that the temperature difference between WT-out and ST is more pronounced in the latter case, with ST being raised by only 15.49 °C, while the temperature difference increases to 1.78 times that of the former. This also proves that the energy brought by the heat flow from the outer surface of the coil is fully utilized under 75% heating load. The increase in heating load causes a higher flame height for combustion and WT-out of the top coil is raised rapidly, but the radiation losses on the outer wall of the coil are likewise increased, so the increase in ST is not significant. So 75% heating load is already sufficient to meet the heat storage target of the MSF.

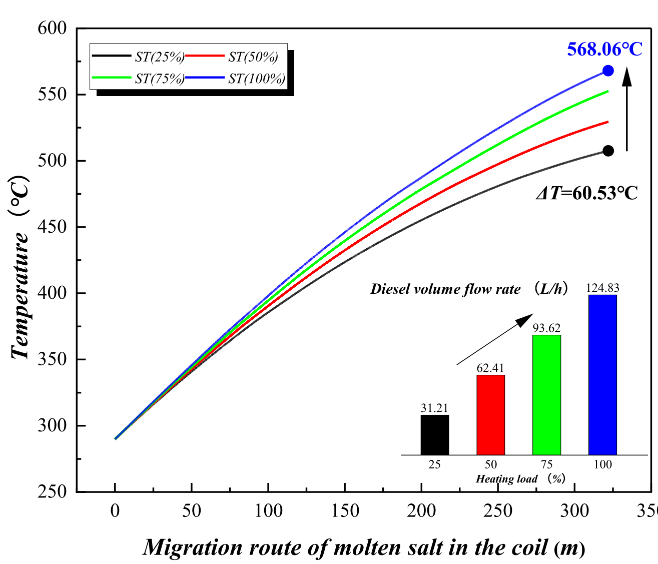

Fig. 15. ST variation at different heat flux densities.

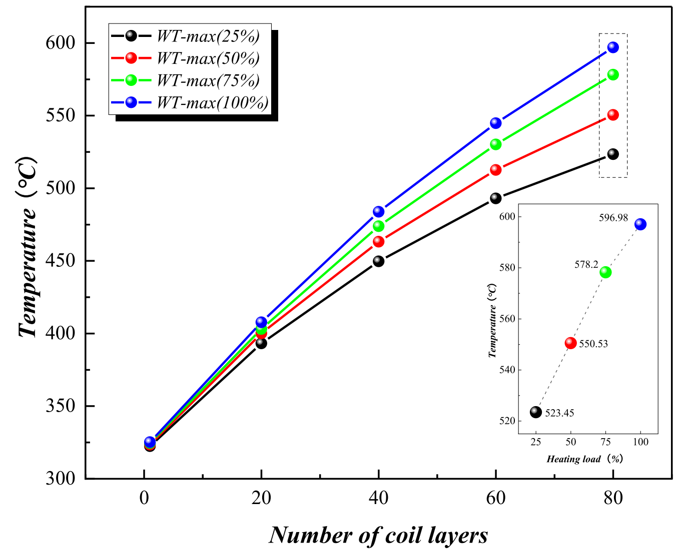

Fig. 16. Distribution of the WT-max at θ = 0° under different loads.

As expected, a higher load results in a higher heat flow density, which leads to a higher temperature on the FW, and a greater difference between WT-out and WT-in. The enhanced heat transfer between the MS and the coil wall results in the MS being heated to higher temperatures. This is in agreement with the simulation results of Marugán-Cruz et al. [56] who concluded that for high *Biot* numbers ($Bi = h{\cdot}e/k_s$, where h is the convective heat transfer coefficient in the tube, e is the tube thickness and k_s is the tube thermal conductivity), the radial heat flow density dominates the effect on the fluid temperature inside the tube.

To further analyze the similarities and differences between the 75% heating load case and the 100% heating load case, the circumferential temperature of the cross-section is examined, as shown in Fig. 12. Since the coil wall on the FW does not receive flame radiation, the WT on the RW is mainly influenced by the ST. And the ST evolution under both radiation flux distributions has a similar trend, so the WT fluctuation at the 180° position is smaller. With the increase of the coil layer, the WT-out of each angle rises, with an average increase of 239.32 °C. The WT-out of the same layer at the 0° position is the highest because the 0° position is the FW, which directly receives the radiation heat flow generated by the burner flame. The 180° position is the lowest in both cases above, at most 31.12 °C and 35.90 °C lower than the 0° position respectively. The increase in load did not increase the temperature difference in the circumferential temperature of the coils and the performance of the two cases above is consistent. So the analysis thereafter will be done with the 75% heating load as the benchmark case for further study and variable operating conditions.

The MS flows into the coil at 1.7 kg/s at the inlet and is discharged at the outlet after 184.80 s. In Fig. 13, different flow times correspond to different temperatures in the MS chamber. The temperature distribution curves of the MS chamber at the 175th and 200th s are basically the same, which is an indication that the simulation reaches a steady state after 200 s, as shown in Fig. 13(a). When the MS is about to enter the coil (0 s), the coil has been heated with a low heating load to complete a good preheating, which makes the temperature of the MS chamber kept above 290 °C, ensuring that the MS will not be condensed. As the MS flows, the heat is first transferred continuously from the bottom layer of the coil to the MS, leading to a continuous decrease in the temperature of the MS chamber in the bottom layer. Due to the increase in the heating load, the temperature of the MS chamber that has not yet passed through the MS increases. After 200s, the temperature of the MS chamber stabilizes as the MS flows continuously, and the heating load becomes stable. Fig. 13(b) shows a more detailed process of MS flow and the dynamic changes in coil temperature, indicating that the temperature

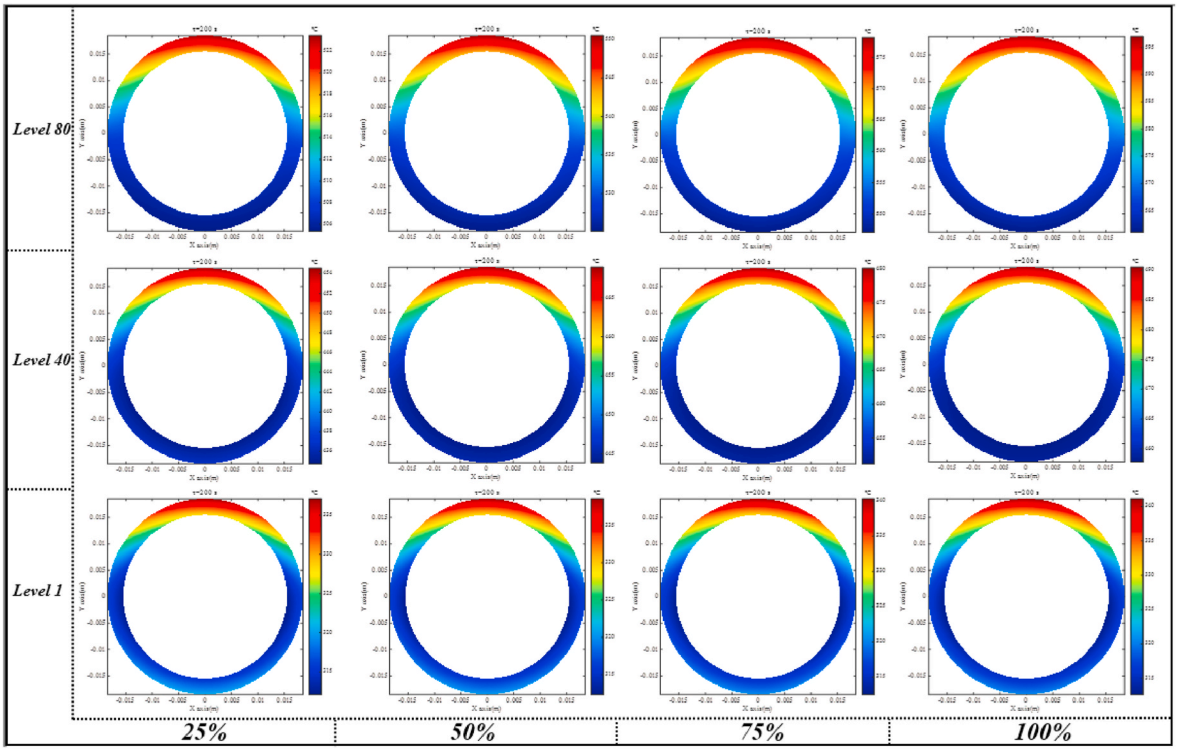

Fig. 17. Cloud diagram of temperature distribution of coil cross-section under different heating loads (1st, 40th and 80th layers as examples).

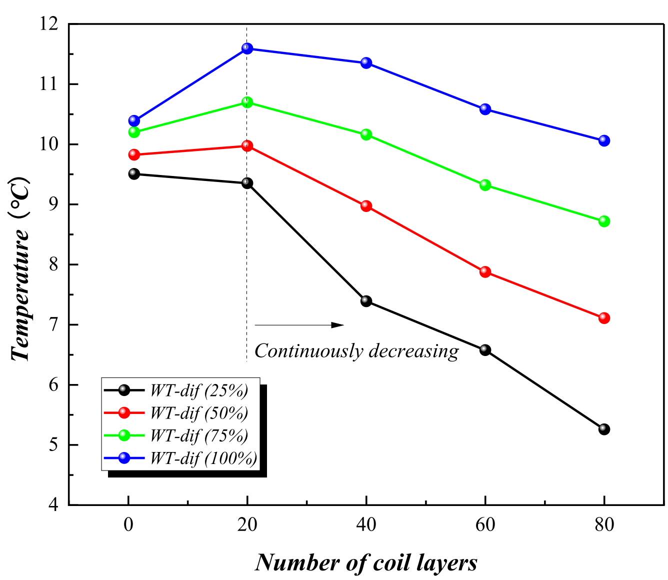

Fig. 18. Maximum temperature difference distribution on the coil wall.

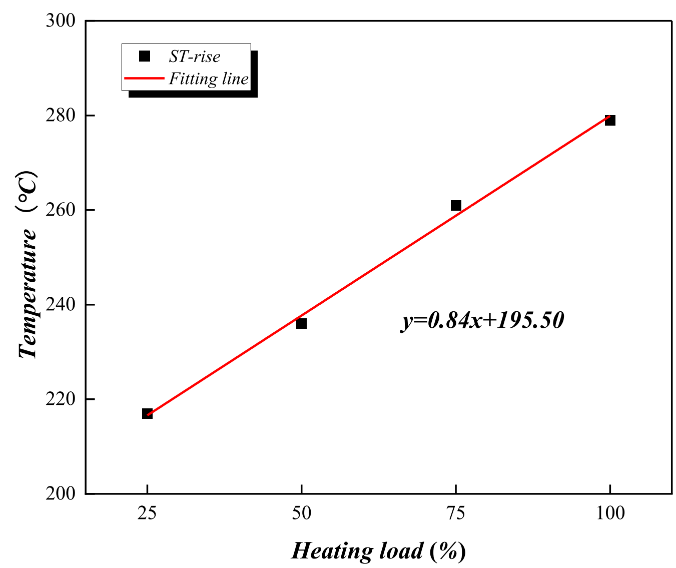

Fig. 19. Data fitting of the ST-rise at different heating load.

decreases when the MS flows through the middle and below of the coil (1st-40th layers).

The temperature distribution cloud diagram of the 40th layer coil cross-section is painted in Fig. 14. The cross-sectional temperature distribution is symmetrical along the line from 0° to 180°, which is since the outer diameter of the coil is only 38 mm and the difference in heat flux density on the FW is very small. The temperature at the same angle decreases gradually with the extension of the thickness of the coil. The temperature on the FW is significantly higher than that on the RW, and the presence of the flue gas reflux chamber ensures that the temperature difference in the cross-section is kept within 30 °C. If there is no secondary heating of the flue gas return chamber, the heat loss on the outer wall surface of the return side is serious, and the temperature difference between the two sides will accelerate the fatigue damage of the coil, and fatigue fracture may occur.

4.4.2. Different heat flux density

The ST-inlet (290 °C) and the SR-inlet (1.7 kg/s) in the benchmark case are kept constant. The heating power (25%, 50%, 75% and 100%) is changed by adjusting the inlet flow rate of the fuel, which in turn changes the heat flux density on FW.

The MS is gradually heated in the coil by accepting the energy transferred from the inner wall. Fig. 15 reveals that the rising trend of the ST under each heating load is basically the same, and the rising speed

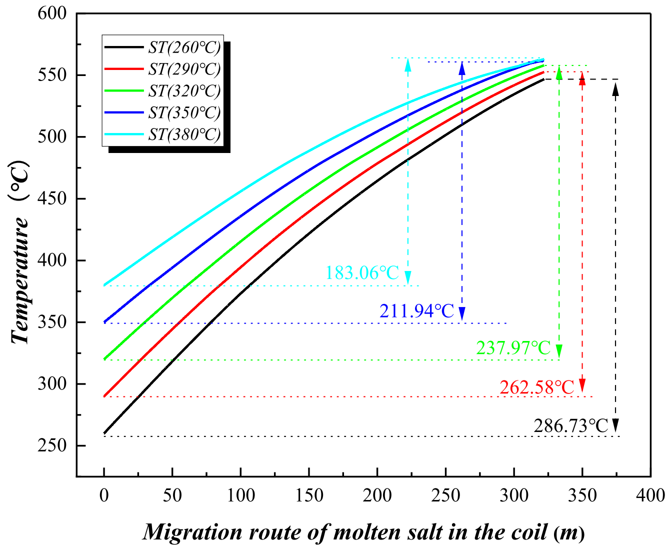

Fig. 20. ST variation at different ST-inlet.

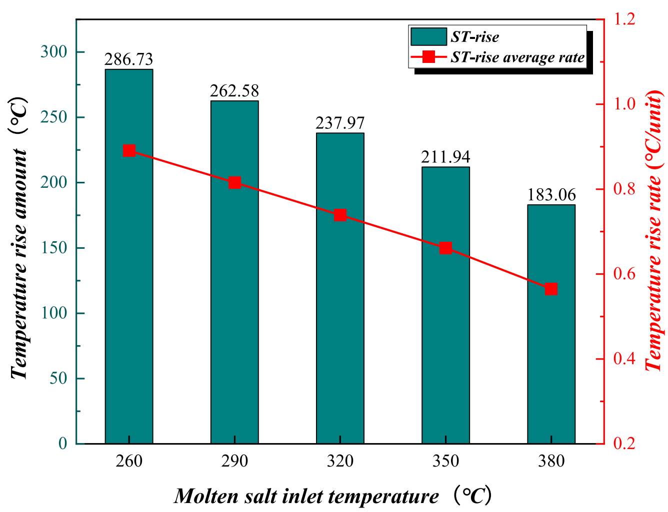

Fig. 21. ST-rise and the ST-rise average rate.

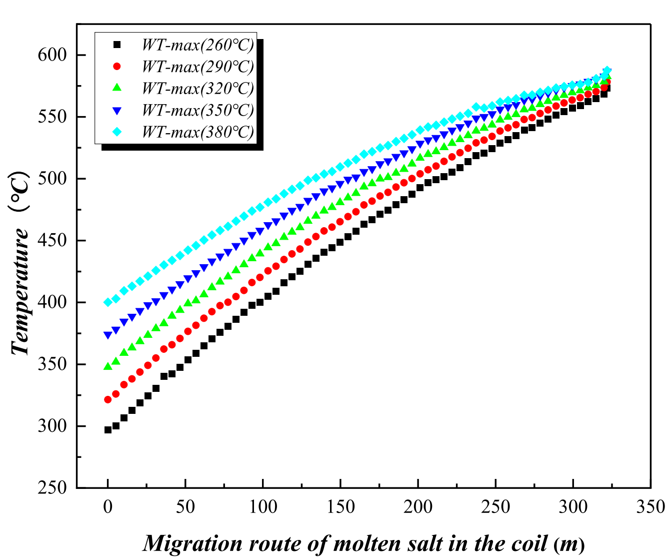

Fig. 22. Distribution of the WT-max at $\theta = 0^\circ$ for different ST-inlet.

gradually slows down. The ST increases with the increase of the heating load, where the temperature can be heated to 568.06 °C under 100% heating load, while 25% heating load can only heat the MS to 507.53 °C, which is lower by 60.53 °C.

The WT-max of the coil cross-section occurs at position θ = 0°. Fig. 16 selects WT at θ = 0° in the 1st, 20th, 40th, 60th, and 80th layers to analyze the distribution of the WT-max at different coil locations. The WT at θ = 0° is consistent with the trend of ST variation, and it is noteworthy that the highest layer (80th layer) temperature increases with the increase of heating load by up to 73.53 °C, which is a 14.05% enhancement.

The above analysis of the temperature distribution in the cross-section of the coil can be confirmed in Fig. 17. It shows the temperature cloud diagram of the coil cross-section for different heating loads (1st, 40th and 80th layers as examples).

The WT-out is higher than WT-in at the same angle, and the temperature of the FW of the same layer is the highest. The heat is gradually transferred to the inner side of the coils and the reflux side, and the temperature of the reflux side is the lowest.

The maximum temperature difference on the coil (WT-dif) for different loads is collected in Fig. 18. As heat is transferred from the outer wall to the inner wall, a certain amount of energy is lost, and the WT-dif of each layer is less than 12 °C. After the 20th layer, the WT-dif will be gradually reduced to a minimum of 5.26 °C. As the heating load decreases, the WT-dif decreases more, up to 5.26 °C, which is 44.59% lower than the maximum value. This indicates that reducing the heating load is beneficial to reduce the loss in the heat transfer process of the coil wall.

From the fitted straight line of temperature rise of molten salt (ST-rise) and heating load in Fig. 19. The ST-rise is linearly related to the heating load. The magnitude of the heat flux density can be significantly changed by adjusting the heating load, thus controlling the ST-rise.

4.4.3. Different ST-inlet

The SR-inlet (1.7 kg/s) and the heat flux density (at 75% heating power) on the FW in the benchmark case are kept constant. The effect on the MSF thermal performance is studied by varying the ST-inlet (260 °C, 290 °C, 320 °C, 350 °C, 380 °C).

As shown in Fig. 20, the MS is gradually heated during the flow in the coil. The ST-inlet change does not affect the overall trend of the MS heating. The ST-outlet reaches a maximum of 563.06 °C at an ST-inlet of 380 °C, while the MS can still be heated to 546.73 °C at an ST-inlet of 260 °C. The ST-outlet increases with the ST-inlet increase, but after the ST-inlet increases above 350 °C, the ST-outlet stabilizes at 565 °C. Conversely, the ST-rise decreases with increasing ST-inlet, from 286.5 °C to 183 °C. In general, when the ST-inlet rises, the WT becomes higher, and the radiative heat loss from the coil increases, which leads to less energy absorption by the MS. So when the heat flow on the coil surface is constant, the temperature rise of the MS decreases as the ST-inlet rises, and this law should be consistent with some simulation results about the heat absorption tube of the solar receiver [26,27,33].

Fig. 21 illustrates that the ST-rise and the ST-rise average rate decrease as the ST-inlet is increased, and it is because the increase in coil temperature leads to an increase in radiant heat loss, which leads to a decrease in the amount of heat available for the MS to absorb. Therefore, if the SR-inlet and the heat flux density on the FW remain unchanged, increasing the ST-inlet leads to a decrease in the ST-rise and a decrease in the MSF thermal performance.

In Fig. 22, the increasing trend of the WT-max at $\theta = 0^\circ$ is consistent with the trend of the ST-rise analyzed previously. The WT-out is heated to over 545 °C at the MS outlet at different ST-inlet. The ST-inlet increase raises the WT-max of the entire coil. When the ST-inlet is raised by 120 °C, the ST-outlet is raised by only 17 °C. Similarly, the WT-max at the MS outlet is raised by 15 °C or less. The cause of these phenomena is also an increase in radiant heat loss. The Nusselt number correlation plays an important role in the WT [31], while the increase in the ST-inlet

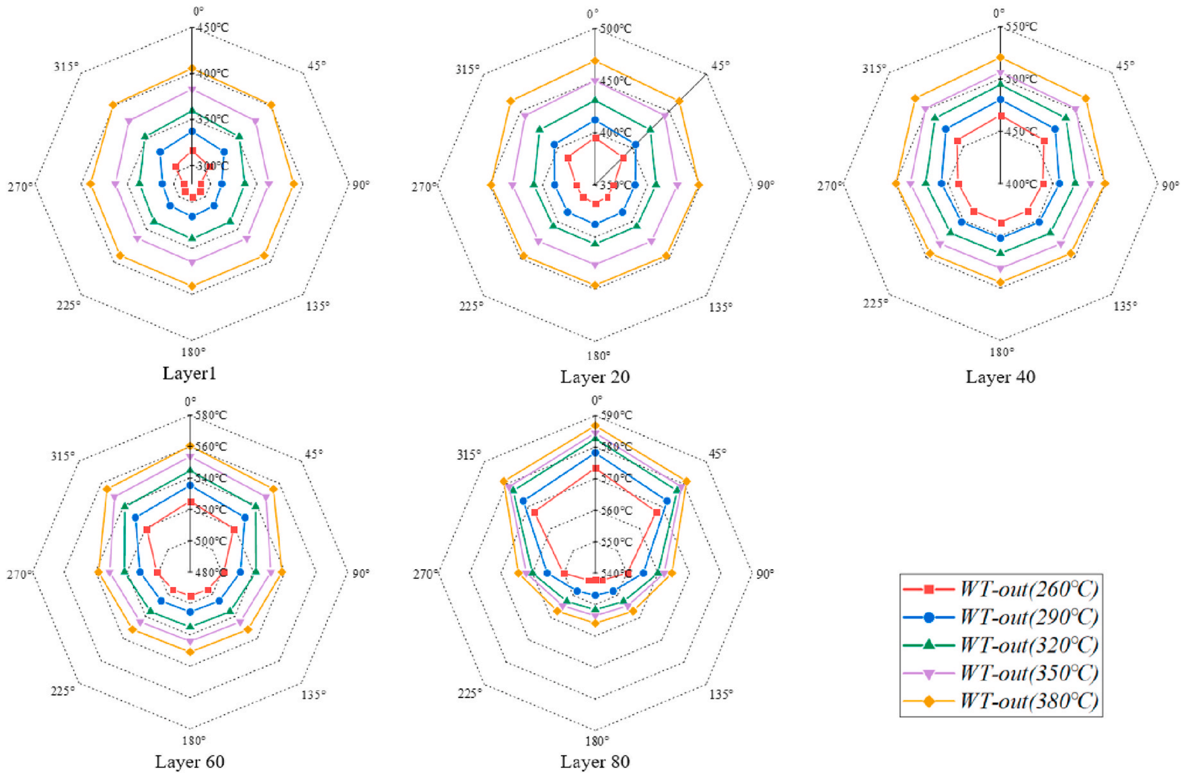

Fig. 23. Coil circumferential WT-out evolution of different layers at different ST-inlet.

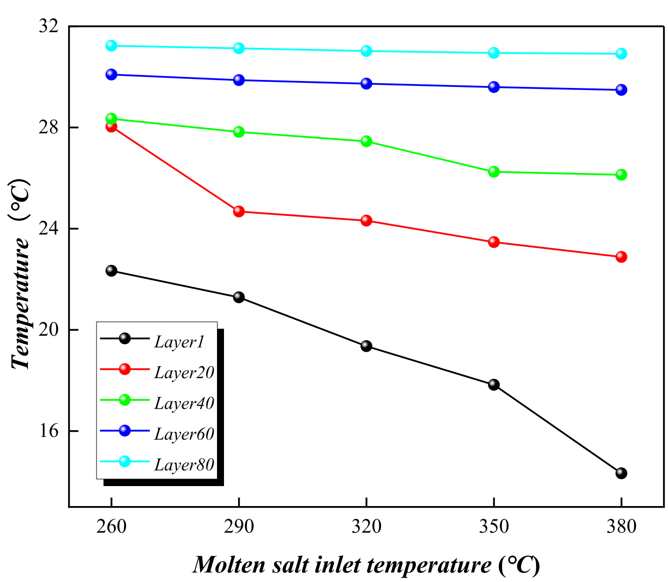

Fig. 24. Coil circumferential WT-dif distribution.

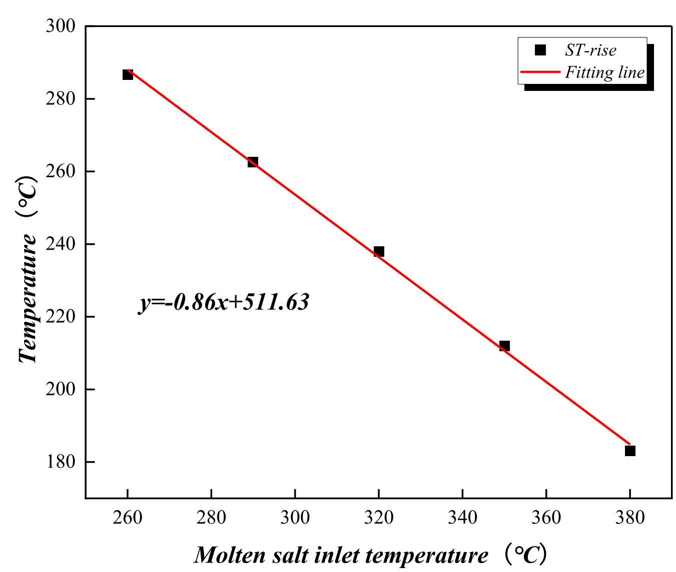

Fig. 25. Data fitting of the ST-rise at the different ST-inlet.

causes a change in the correction parameter in the correlation of forced convection in the coil, as shown by the decrease in the viscosity of the MS with the increase in temperature, which leads to a higher flow rate of the MS near the wall and enhances the heat transfer between the coil and the MS. On the other hand, the decrease in temperature difference between the MS and the coil leads to a decrease in the heat transfer coefficient, and from the simulation results obtained, the effect of temperature difference on the WT is more obvious.

From Fig. 23, it can be obtained that the coil circumferential WT-out evolution of different layers at different ST-inlet. The WT-out of all angles increases as the MS flows through more coil layers, but the WT-dif becomes prominent and can reach 32.23 °C. The temperature distribution of the bottom coil is more even, and the WT-dif is within 22.50 °C. The above analysis indicates that increasing the ST-inlet will lead to an enormous temperature difference in the top coils.

However, increasing the ST-inlet also brings some benefits, namely, it can improve the circumferential WT-dif of the bottom coil, as evidenced by the data in Fig. 24. Especially, the circumferential WT-dif of the coil below the 20th layer can be reduced by up to 35.91% with the increase of the ST-inlet, which can reduce the thermal stress on the coil. A moderate increase in the ST-inlet contributes significantly to the stable operation and longevity of the MSF.

As seen in Fig. 25, there is a linear relationship between the ST-rise

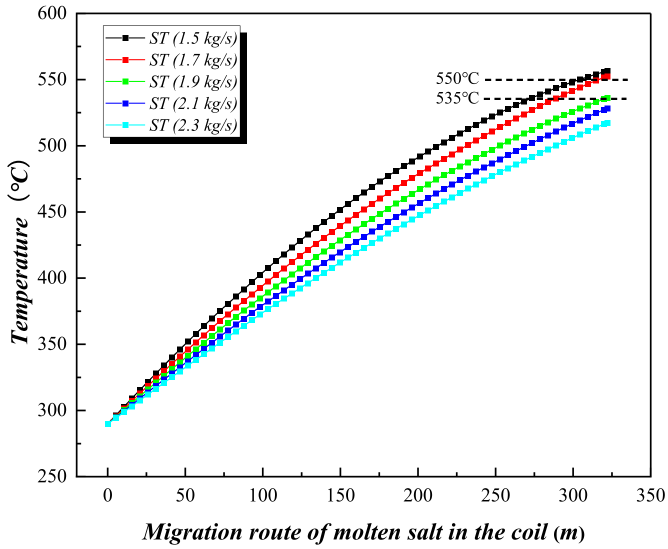

Fig. 26. ST variation at different SR-inlet.

and the ST-inlet. The higher the ST-inlet, the smaller the ST-rise. As the ST-inlet increases, the WT generally rises while the ST decreases. Because under constant heating load, the increase of WT raises the heat loss of the coil, reducing the temperature difference between the WT and the ST, thus making it more challenging to increase the ST.

4.4.4. Different SR-inlet

The SR-inlet variation has a significant impact on the MSF thermal performance. As switching the heating load during the MSF operation is quite common, the WT stability is generally ensured by adjusting the SR-inlet on site.

The ST-inlet (290 °C) and the heat flux density (75% heating power) on the FW in the benchmark case are kept constant. The effect on the MSF thermal performance is studied by varying the SR-inlet (1.5 kg/s, 1.7 kg/s, 1.9 kg/s, 2.1. kg/s and 2.3 kg/s).

Fig. 26 shows the variation curve of the ST during the flow migration. The ST-rise is significantly affected by the SR-inlet. When the SR-inlet is less than 1.7 kg/s, the ST-outlet exceeds 550 °C. However, when the SR-inlet exceeds 1.9 kg/s, the ST-outlet is less than 535 °C, decreasing the MSF heating efficiency. This also confirms the claim by Yu et al. [29] that an upward (downward) perturbation of the molten salt mass flow rate will result in a gradual decrease (increase) in the molten salt outlet temperature.

Fig. 27 presents the coil circumferential WT-out evolution of different layers at different SR-inlet. The WT-out of each layer shows a continuous decrease from 0° to 180° and a continuous increase from 180° to 360°, and the particular 1st layer will be interpreted separately.

With the SR-inlet increase, the WT-out of each layer in the cross-section is significantly increased, and the 60th layer has the highest increase of 45.89 °C. This indicates that the upper-middle layers of the coil are more sensitive to the SR-inlet, and the temperature fluctuation at the $\theta = 0°$ position of the same layer is the most obvious. With the

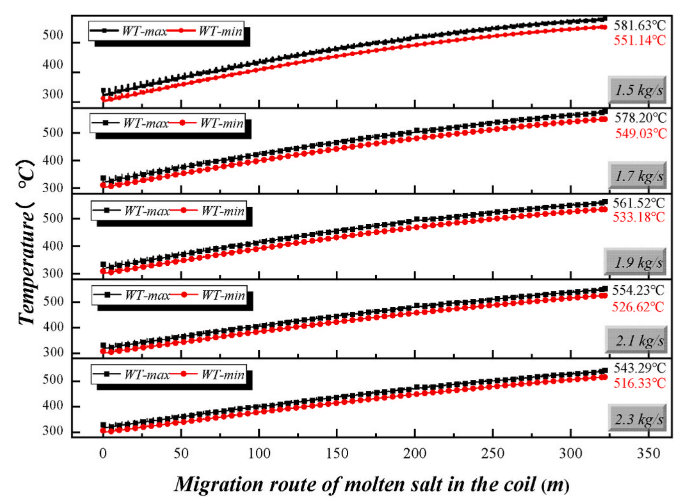

Fig. 28. Distribution of WT-max and WT-min at different SR-inlet.

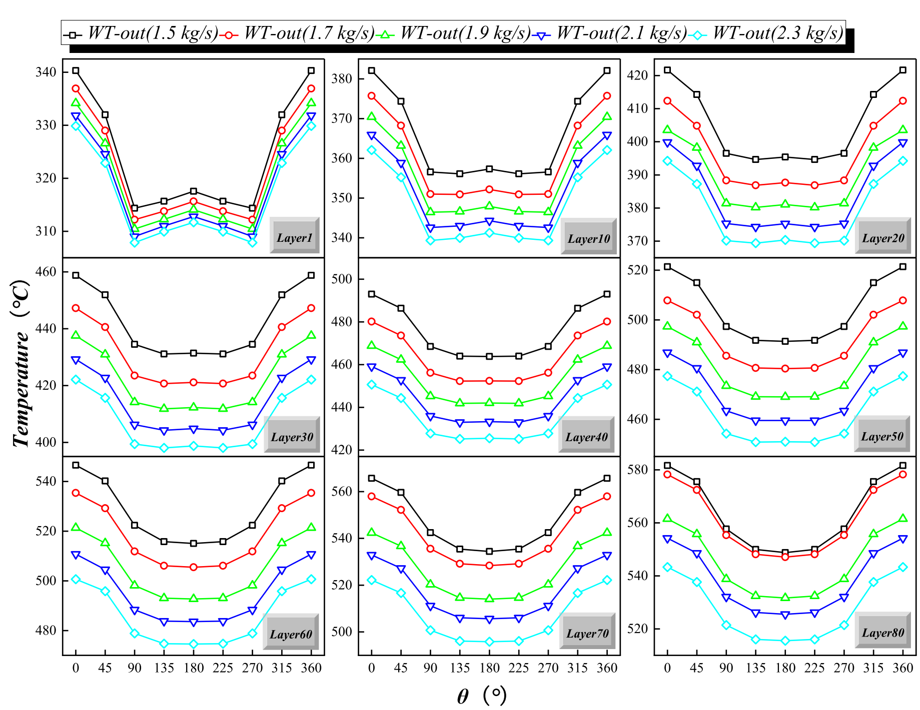

Fig. 27. Coil circumferential WT-out evolution of different layers at different SR-inlet.

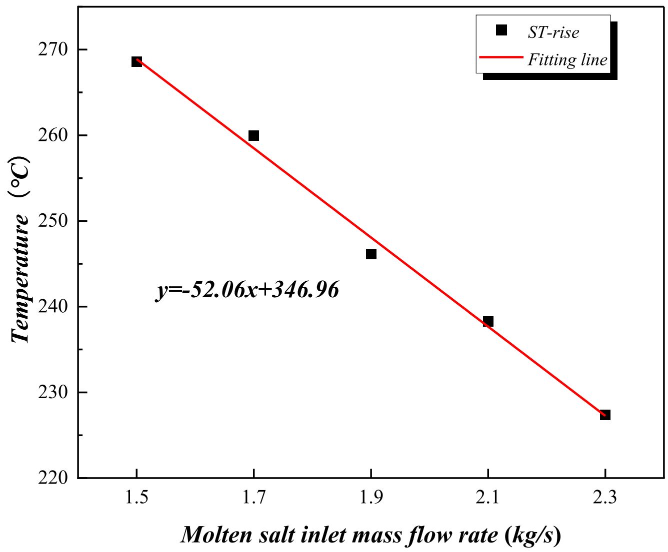

Fig. 29. Data fitting of the ST-rise at different SR-inlet.

increase of the number of layers, the WT-out at each angle in the cross-section is increased, with the slowest increase at $\theta = 180^\circ$ and the fastest increase at $\theta = 0^\circ$. It is worth noting that WT-out is lowest at $\theta = 90^\circ$ at the 1st layer, which is due to the uneven distribution of heat flux density resulting in a lower heat flux density on the FW of 1st layer, thus allowing the convective heat transfer effect of the flue gas return chamber to be reflected. This proves that the presence of the flue gas return chamber facilitates the uniform temperature distribution in the bottom coil.

The distribution of the WT-max and the WT-min at different SR-inlet are statistically presented in Fig. 28. As the SR-inlet increased from 1.5 kg/s to 1.7 kg/s, the WT-max and the minimum wall temperature (WT-min) at the MS outlet both decreased significantly, by 38.34 °C and 34.81 °C respectively. The reason is that as the SR-inlet increases without changing the heat flux density, the heat transfer coefficient between the MS and the inner wall of the coil increases. Moreover, the ST in contact with the inner wall decreases at every position of the coil, resulting in more heat carried away by the MS in the same amount of time, leading to a decrease in the WT. Increasing the SR-inlet by 0.8 kg/s can reduce the WT-out by 6.59%. These results are in agreement with the numerical results of Flores et al. [57] and the CFD results of Yang et al. [58], who both indicated that the increase in fluid flow velocity in the tube enhances the heat transfer between the fluid and the wall. Therefore, when the heating load has problems and the heat flow is abnormal, the overall WT can be ensured not to exceed the upper limit by changing the SR-inlet. This is an effective and convenient method to ensure the security of the MSF.

Fig. 29 shows a linear relationship between the ST-rise and the SR-inlet. The ST-rise increases with increasing SR-inlet. Changing the SR-inlet is the simplest and most convenient way to ensure that the WT is at a safe level during operation. The above conclusions support the operation of the MSF in the field.

5. Conclusion

In this paper, a three-dimensional transient thermal performance calculation program for the MSF is developed using MATLAB. The program loads the heat flux density distribution simulated by ANSYS FLUENT and can quickly obtain the detailed distribution of the WT and the ST. An experimental platform of a laboratory-scale MSF (1.05 MW) is constructed and a heat storage experiment is conducted on the benchmark case to verify the accuracy of the procedure. This program explores the transient MSF thermal performance under changing heat flux density, ST-inlet, and SR-inlet. The main conclusions are as follows:

(1) In the benchmark case experiment, the experimental ST-out is measured as 566.5 °C, which is 13.92 °C higher than the simulated data, with a deviation of 2.46%. The temperature of 10 measurement points on the coil wall is in good agreement with the corresponding simulated temperatures, with an average deviation of 2.90% and a minimum temperature difference of only 1.9 °C. These results indicate that the proposed calculation model is accurate.
(2) The increase in the heating load of the MSF leads to a higher heat flux density, which in turn results in a higher ST-rise. Among them, under a 100% heating load, the MS can be heated to 568.06 °C, while under a 25% heating load, the MS can only be heated to 507.53 °C, which is reduced by 60.53 °C.
(3) The change of the ST-inlet does not affect the MS heating process trend, and MS is heated up to 563.06 °C when the ST-inlet is 380 °C. Even when the ST-inlet is 260 °C, the MS can still be heated to 546.73 °C. The increase of ST-inlet will reduce the MSF thermal performance.
(4) The SR-inlet significantly affects the coil temperature fluctuation. Increasing the SR-inlet by 0.8 kg/s can reduce the WT-out by 6.59%. When the heat flux on the coil is abnormal, adjusting the SR-inlet can ensure that the coil temperature is within a safe range. The presence of the flue gas return chamber facilitates uniform temperature distribution in the bottom coil thus reducing fatigue damage to the coil.
(5) The ST-rise is linearly related to the heating load, the ST-inlet, and the SR-inlet. Increasing the heating load will increase the ST-rise. On the other hand, an increase in the ST-inlet and SR-inlet will decrease the ST-rise. In summary, reasonable adjustment of the SR-inlet is a convenient and powerful measure to ensure the safety of the coil temperature.

Author contribution

Xue Xue: Conceptualization, Writing - review & editing, Visualization, Supervision, Xiang Liu: Methodology, Software, Validation, Yifan Zhu: Methodology, Validation, Lei Yuan: Mathematical model, Ying Zhu: Mathematical model, Kelang Jin: Formal analysis, Investigation, Data curation, Lei Zhang: Formal analysis, Data curation, Hao Zhou: Project administration, Funding acquisition, Formal analysis, Investigation.

Declaration of competing interest

The authors declare that they have no known competing financial interests or personal relationships that could have appeared to influence the work reported in this paper.

Data availability

Data will be made available on request.

Acknowledgments

This work was supported by the Fundamental Research Funds for the Central Universities (2022ZFJH04).

Nomenclature

Roman symbols

C_p	constant-pressure specific heat J/(kg·°C)
T	temperature (°C)

Greek symbols

α	thermal diffusivity (m^2/s)
λ	thermal conductivity (W/(m·°C))
μ	dynamic viscosity (Pa·s)
ρ	density (kg/m^3)

Abbreviation

BFG	blast furnace gas
CCUS	carbon capture, utilization and storage
COG	coke oven gas
CFD	computational fluid dynamics
CSP	concentrated solar power
DO	discrete-ordinates Method
FW	outer wall surface of the coil toward the fire
PDF	probability density function
MS	molten salt
MSF	molten salt furnace
MSFTES	molten salt furnace thermal energy storage
RW	outer wall surface of the coil reflux side
SR-inlet	molten salt inlet mass flow rate
ST	molten salt temperature
ST-inlet	molten salt inlet temperature
ST-outlet	molten salt outlet temperature
ST-rise	temperature rise of molten salt
TES	thermal energy storage
WT	coil wall temperature
WT-dif	maximum temperature difference on the coil
WT-in	inner wall temperature
WT-max	maximum wall temperature of the coil
WT-min	minimum wall temperature of the coil
WT-out	outer wall temperature

References

[1] Zhang N, Lior N, Jin H, Lund H, Kaiser MJ. The energy situation and its sustainable development strategy in China. Energy 2011;36(6):3639–49.
[2] Li Q, Li C, Du Z, Jiang F, Ding YJAE. A review of performance investigation and enhancement of shell and tube thermal energy storage device containing molten salt based phase change materials for medium and high temperature applications. Appl Energy 2019;255(Dec.1). 113806.1-.37.
[3] Kim J, Sovacool BK, Bazilian M, Griffiths S, Lee J, Yang M, et al. Decarbonizing the iron and steel industry: a systematic review of sociotechnical systems, technological innovations, and policy options. Energy Res Social Sci 2022;89:102565.
[4] Griffin PW, Hammond GP. The prospects for 'green steel' making in a net-zero economy: a UK perspective. Global Transitions 2021;3:72–86.
[5] Zhang J, Shen J, Xu L, Zhang Q. The CO_2 emission reduction path towards carbon neutrality in the Chinese steel industry: a review. Environ Impact Assess Rev 2023;99:107017.
[6] Hornby GABA. Alternate routes to green steel. 2022.
[7] Shahabuddin M, Brooks G, Rhamdhani MA. Decarbonisation and hydrogen integration of steel industries: recent development, challenges and technoeconomic analysis. J Clean Prod 2023;395:136391.
[8] Zhang N, Lior N, Jin H. The energy situation and its sustainable development strategy in China. Energy 2011;36(6):3639–49.
[9] Abdul Quader M, Ahmed S, Dawal SZ, Nukman Y. Present needs, recent progress and future trends of energy-efficient Ultra-Low Carbon Dioxide (CO_2) Steelmaking (ULCOS) program. Renew Sustain Energy Rev 2016;55:537–49.
[10] Kong R, Zhang R, Li H, Wu Y, Sun Z, Sun Z. A new pathway to produce hydrogen with COx capture from blast furnace gas via SOFC-SOEC integration. Energy Convers Manag 2022;271:116278.
[11] Yoon T-U, Kim MJ, Kim A-R, Kang JH, Ji D, Bae Y-S. Cu-impregnated metal–organic frameworks for separation and recovery of CO from blast furnace gas. J Ind Eng Chem 2020;87:102–9.
[12] Porter RTJ, Cobden PD, Mahgerefteh H. Novel process design and techno-economic simulation of methanol synthesis from blast furnace gas in an integrated steelworks CCUS system. J CO2 Util 2022;66:102278.
[13] Lukashuk L, van de Water LGA, van Dijk HAJ, Cobden PD, Dodds DL, Hyde TI, et al. A new application of the commercial high temperature water gas shift catalyst for reduction of CO_2 emissions in the iron and steel industry: lab-scale catalyst evaluation. Int J Hydrogen Energy 2021;46(79):39023–35.
[14] Liu L, Jiang Z, Zhang X, Lu Y, He J, Wang J, et al. Effects of top gas recycling on in-furnace status, productivity, and energy consumption of oxygen blast furnace. Energy 2018;163:144–50.
[15] Kenisarin MM. High-temperature phase change materials for thermal energy storage. Renew Sustain Energy Rev 2010;14(3):955–70.
[16] Liu M, Tay N, Bell S, Belusko M, Jacob R, Will G, et al. Review on concentrating solar power plants and new developments in high temperature thermal energy storage technologies. Renewable Sustainable Energy Rev 2016;53(JAN):1411–32.
[17] Dong X, Bi Q, Jiang J, Jiang M. Experimental investigation on the shell-side heat transfer performance of molten salt steam generator. Int J Heat Mass Tran 2020;158(5):119991.
[18] Wei G, Gang W, Chao X, Xing J, Xing L, Du X, et al. Selection principles and thermophysical properties of high temperature phase change materials for thermal energy storage: a review. Renew Sustain Energy Rev 2018;81:1771–86.
[19] Xinhai Arvay A, Hsu K, Kannan, et al. Heat transfer fluids for concentrating solar power systems - a review. Appl Energy 2015.
[20] Wang W-Q, Li M-J, Cheng Z-D, Li D, Liu Z-B. Coupled optical-thermal-stress characteristics of a multi-tube external molten salt receiver for the next generation concentrating solar power. Energy 2021:233.
[21] Zhang S, Liu M, Zhao Y, Liu J, Yan J. Energy and exergy analyses of a parabolic trough concentrated solar power plant using molten salt during the start-up process. Energy 2022;254:124480.
[22] Wang WQ, Qiu Y, Li MJ, He YL, Cheng ZD. Coupled optical and thermal performance of a fin-like molten salt receiver for the next-generation solar power tower. Appl Energy 2020:272.
[23] Zou C, Zhang Y, Falcoz Q, Neveu P, Zhang C, Shu W, et al. Design and optimization of a high-temperature cavity receiver for a solar energy cascade utilization system. Renew Energy 2017;103:478–89.
[24] Zou C, Zhang Y, Feng H, Falcoz Q, Neveu P, Gao W, et al. Effects of geometric parameters on thermal performance for a cylindrical solar receiver using a 3D numerical model. Energy Convers Manag 2017;149:293–302.
[25] Zhou H, Li Y, Zhou M, Liu D, Zhu Y, Fang W. Numerical simulation of a lab-scale molten-salt external solar receiver and its experimental validation. J Energy Eng 2021;147(1).
[26] Zhou H, Li Y, Zhu Y, Fang W, Liu D, Zhou M, et al. Experimental and numerical evaluation of a lab-scale external solar receiver. J Renew Sustain Energy 2020;12(4).
[27] Zhou H, Li Y, Zuo Y, Zhou M, Fang W, Zhu Y. Thermal performance and thermal stress analysis of a 600 MWth solar cylinder external receiver. Renew Energy 2021;164:331–45.
[28] Yao L, Xiao X, Wang Y, Yao X, Ma Z. Dynamic modeling and hierarchical control of a concentrated solar power plant with direct molten salt storage. Energy 2022:252.
[29] Yu Q, Fu P, Yang Y, Qiao J, Wang Z, Zhang Q. Modeling and parametric study of molten salt receiver of concentrating solar power tower plant. Energy 2020;200.
[30] Rodríguez-Sánchez M, Marugan-Cruz C, Acosta-Iborra A, Santana D. Comparison of simplified heat transfer models and CFD simulations for molten salt external receiver. Appl Therm Eng 2014;73(1):993–1005.
[31] Fritsch A, Uhlig R, Marocco L, Frantz C, Flesch R, Hoffschmidt B. A comparison between transient CFD and FEM simulations of solar central receiver tubes using molten salt and liquid metals. Sol Energy 2017;155:259–66.
[32] Albarbar A, Arar A. Performance assessment and improvement of central receivers used for solar thermal plants. Energies 2019;12(16).
[33] Xu L, Stein W, Kim J-S, Too YCS, Guo M, Wang Z. Transient numerical model for the thermal performance of the solar receiver. Appl Therm Eng 2018;141:1035–47.
[34] Dong X, Bi Q, Jiang J, Jiang M. Experimental investigation on the shell-side heat transfer performance of molten salt steam generator. Int J Heat Mass Tran 2020:158.
[35] Huang Z, Zou Y, Ding J, Lu J. Experimental investigation of heat transfer in coiled tube type molten salt steam generator. Appl Therm Eng 2019;148:1131–8.
[36] Ning L, Fu D, Zhou CQ, Zhou J. Numerical simulation and optimization of the thermodynamic process of the molten salt furnace. J Therm Sci Eng Appl 2015;7(1).
[37] Wang J, Li Y, Zhang J. Coordinated control of concentrated solar power systems with indirect molten salt storage considering operation mode switching: using switching model predictive control. Energy 2023;268:126686.
[38] Yang H, Li J, Huang Y, Kwan TH, Cao J, Pei G. Feasibility research on a hybrid solar tower system using steam and molten salt as heat transfer fluid. Energy 2020;205:118094.
[39] Zhang Q, Li X, Wang Z, Zhang J, El-Hefni B, Xu L. Modeling and simulation of a molten salt cavity receiver with Dymola. Energy 2015;93:1373–84.
[40] Liu X, Shi X, Li Y, Ye L, Wei X, Zhu S, et al. Synthetic salt rock prepared by molten salt crystallization and its physical and mechanical properties. Energy 2023:269.
[41] Ruan Z-H, Gao P, Yuan Y, Tan H-P. Theoretical estimation of temperature-dependent radiation properties of molten solar salt using molecular dynamics and first principles. Energy 2022;246:123379.
[42] Zavoico. Solar power tower design basis document, revision 0. Office of Scientific Technical Information Technical Reports; 2001.
[43] Khazaei KA, Hamidi AA, Rahimi M. Numerical investigation of fuel dilution effects on the performance of the conventional and the highly preheated and diluted air combustion furnaces. Chin J Chem Eng 2009;17(5):711–26.
[44] Tsan-Hsing S, William WL, Aamir S. A new k-ε eddy viscosity model for high Reynolds number turbulent flows: model development and validation. Comput Fluid 1995;24(3).
[45] Ventura C, Azevedo J. Development of a numerical model for natural gas steam reforming and coupling with a furnace model. Int J Hydrogen Energy 2010;35(18):9776–87.
[46] Yang W, Blasiak W. Numerical simulation of properties of a LPG flame with high-temperature air. Int J Therm Sci 2005;44(10):973–85.
[47] Ebrahimnia-Bajestan E, Khatibi M, Wood D, Maadi SR. Coupled thermal-optical numerical modeling of PV/T module – combining CFD approach and two-band radiation DO model. Energy Convers Manag 2019;198:111781.

[48] M C, Sharatchandra Mihir, Sen Mohamed, et al. Discrete-ordinates solution of radiative transfer equation in nonaxisymmetric cylindrical enclosures. J Thermophys Heat Tran 1992.
[49] Wang W-Q, Li M-J, Jiang R, Cheng Z-D, He Y-L. A comparison between lumped parameter method and computational fluid dynamics method for steady and transient optical-thermal characteristics of the molten salt receiver in solar power tower. Energy 2022:245.
[50] Fernandez-Torrijos M, Sobrino C, Almendros-Ibanez JA, Marugan-Cruz C, Santana D. Inverse heat problem of determining unknown surface heat flux in a molten salt loop. Int J Heat Mass Tran 2019;139(AUG):503–16.
[51] Huang ZH, Li YW, Zhu YF, Zhou H. Numerical study on the transient thermal performance of a lab-scale molten salt receiver. J Renew Sustain Energy 2022;14 (3):14.
[52] Modest MF. Radiative heat transfer. Int J Heat Mass Tran 2013.
[53] Çengel Yunus A. Heat transfer: a practical approach: heat transfer. A Practical Approach; 2003.
[54] Bejan A, Kraus AD. Heat transfer handbook. Wiley; 2003.
[55] Yang S. WT. Heat transfe, fourth edition. Beijing: Higher Education Press; 2006.
[56] Marugán-Cruz C, Flores O, Santana D, García-Villalba M. Heat transfer and thermal stresses in a circular tube with a non-uniform heat flux. Int J Heat Mass Tran 2016; 96:256–66.
[57] Flores O, Marugán-Cruz C, Santana D, García-Villalba M. Thermal stresses analysis of a circular tube in a central receiver. Energy Proc 2014;49:354–62.
[58] Yang X, Yang X, Ding J, Shao Y, Fan H. Numerical simulation study on the heat transfer characteristics of the tube receiver of the solar thermal power tower. Appl Energy 2012;90(1):142–7.